SAND2018-12595R

FY18 Status Report: SNL Research into Stress Corrosion Cracking of SNF Interim Storage Canisters

Spent Fuel and Waste Disposition

Prepared for
US Department of Energy
Spent Fuel and Waste Science and Technology

C. Bryan
E. Schindelholz

Sandia National Laboratories
September 28, 2018
Milestone No. M2SF-18SN010201049
SAND2018 XXXXXX

Sandia National Laboratories is a multimission laboratory managed and operated by National Technology & Engineering Solutions of Sandia, LLC, a wholly owned subsidiary of Honeywell International Inc., for the U.S. Department of Energy's National Nuclear Security Administration under contract DE-NA0003525.

Prepared by
Sandia National Laboratories
Albuquerque, New Mexico 87185 and Livermore, California 94550

Sandia National Laboratories is a multimission laboratory managed and operated by National Technology and Engineering Solutions of Sandia, LLC, a wholly owned subsidiary of Honeywell International, Inc., for the U.S. Department of Energy's National Nuclear Security Administration under contract DE-NA0003525.

Sandia National Laboratories

SUMMARY

This progress report describes work done in FY18 at Sandia National Laboratories (SNL) to assess the localized corrosion performance of container/cask materials used in the interim storage of spent nuclear fuel (SNF). The work focuses on stress corrosion cracking (SCC), the only mechanism by which a through-wall crack could potentially form in a canister outer wall over time intervals that are shorter than possible dry storage times. Work in FY18 continued several studies initiated in FY17 that are aimed at refining the understanding of the chemical and physical environment on canister surfaces, and evaluating the relationship between chemical and physical environment and the form and extent of corrosion that occurs. The SNL canister environment work focused on evaluating the stability of sea-salt deliquescent brines on the heated canister surface; an additional opportunity to analyze dusts sampled from an in-service spent nuclear fuel storage canister also arose. The SNL corrosion work focused predominantly on pitting corrosion, a necessary precursor for SCC, and process of pit-to-crack transition. SNL is collaborating with several university partners to investigate SCC crack growth experimentally, providing guidance for design and interpretation of experiments. The scope of these efforts targets near-marine Independent Spent Fuel Storage Installation environments which are generally considered to be most aggressive for pitting and SCC.

Work to define the chemical and physical environment that could develop on storage canister surfaces in near-marine environments included experiments to evaluate the thermal stability of magnesium chloride brines, representative of the first brines to form when sea-salts deliquesce, with the specific goal of understanding and interpreting results of sea-salt and magnesium chloride corrosion experiments carried out under accelerated conditions. The experiments showed that magnesium chloride brines, and by extension, low RH sea-salt deliquescent brines, are not stable at elevated temperatures, losing chloride via degassing of HCl and conversion to Mg-hydroxychlorides and carbonates. The experiments were carried out on an inert substrate to eliminate the effects of corrosion reactions, simulating brine stabilities in the absence of, or prior to, corrosion. Moreover, analysis of salts recovered from actively corroding metal samples shows that corrosion also supports or drives conversion of magnesium chloride or sea-salt brines to less deliquescent salts. This process has significant implications on corrosion, as the secondary phases are less deliquescent than magnesium chloride; the conversion reaction results in decreases in brine volume, and potentially results in brine dry-out. The deliquescence properties of these reaction products will be a topic of active research in FY19.

In FY18, Sandia also continued its multi-year study of salts deposited on the surface of in-service SNF interim storage canisters, obtaining and analyzing dust samples from the Maine Yankee site. Soluble salts were present in significant amounts in the dust, and were dominated by sulfates and nitrates. However, chloride was present in significant amounts, occurring as sodium chloride and commonly associated with coarse plant fibers and pollen in the dust, and with fine aggregates of silicate minerals, likely clays. Sea-salt aerosols were not observed. The association of chloride salts with other particulates must be considered when evaluating salt transport and deposition phenomena both externally and within the overpack, as the aerodynamic properties of the materials will vary from those of standard sea-salt aerosols or deliquesced droplets. The composition of the soluble component was relatively consistent in the six samples collected, although the amount present varied. The composition and relative species concentrations (ion ratios) indicate that sea-salts alone cannot account for the observed salts, and that a large component of continental-salt aerosols is present. Measured chloride surface loads are low, with the highest values being less than 0.1 g/m^2. Salt load is an important risk factor for SCC, and while values this low have been known to cause SCC, these low salt loads are a positive factor. The potential role of the other soluble components in mitigating or increasing SCC risk is not known.

Experimental efforts in FY18 to understand the relationship between surface environment and corrosion damage focused on four thrust areas: (1) generation of temporal statistical pitting data as function of environment; (2) hierarchal identification of features controlling pit-to-crack transitions; (3) definition of

the surface environment-electrochemical relationship driving pitting and SCC; (4) definition of relative governance on material condition and stress relative to surface environmental conditions on electrochemical kinetics and SCC susceptibility. FY18 work in area (1) continued with characterization of pitting damage and surface chemistry on 304L coupons loaded with sea-salt and exposed to storage-relevant fixed RH,T conditions. To date, samples exposed for up to 1 year have been generated. In collaboration with Ohio State University (OSU), we have demonstrated a semi-automated pit measurement approach based on optical profilometry and generated initial pit datasets for coupon exposure times up to 6 months. These data will be used to directly test the SNL SCC model and develop statistical models in collaboration with Colorado School of Mines (CSM). Regarding (2), and in collaboration with OSU, experiments have been initiated to identify pit-to-crack transition features. Accomplishments include deposition of salt and exposure of tensile test specimens to the environmental conditions used in thrust (1) for up to six months. Additionally, we have developed and tested a method for periodic loading of the specimens while under said environments. Regarding (3), the cathodic electrochemical kinetics that drive corrosion on stainless steel were measured for NaCl brines as analogs to expected brines compositions on the canisters at the upper end of expected ISFSI surface humidity range. These data were incorporated into SNL's SCC model and findings communicated in a peer-reviewed journal publication. Work in area (4) included completion of 4-point bend experiments using stressed 304L bars loaded with sea salt and exposed to 35%RH, 50ºC conditions in collaboration with CSM. The pit distribution on one of these bars was analyzed via optical profilometry with initial results suggesting pit frequency, depth and diameter was independent on material stress state within expected canister conditions. Finally, we initiated exposure of a salt-loaded mockup canister plates to elevated RH and T conditions to gain understanding on what portions of the canister may be most susceptible to SCC and their relationship to material condition and mechanical environment.

ACKNOWLEDGEMENTS

The authors acknowledge the contributions to this report from Chris Alexander (SNL), Jason Taylor (SNL), Jacob Carpenter (SNL), Bonnie McKenzie (SNL), Steve Meserole (SNL), all at SNL; Jen Locke and Tim Weirich at Ohio State University; and Zhenzhen Yu and Xin Wu at the Colorado School of Mines.

This page is intentionally left blank.

CONTENTS

LIST OF FIGURES

LIST OF TABLES

ACRONYMS

CRIEPI	[Japanese] Central Research Institute of the Electric Power Industry
CSM	Colorado School of Mines
DOE	US Department of Energy
EDS	energy dispersive [X-ray] spectroscopy
EPRI	Electric Power Research institute
FCRD	Fuel Cycle Research and Development
FY	fiscal year
IC	ion chromatography
IRP	integrated research project
ISFSI	independent spent fuel storage installation
NRC	Nuclear Regulatory Commission
ORR	oxygen reduction reaction
OSU	Ohio State University
RH	relative humidity
SCC	stress corrosion cracking
SEM	scanning electron microscope
SFWST	Spent Fuel and Waste Science and Technology
SNF	spent nuclear fuel
SNL	Sandia National Laboratory
TOF-SIMS	time-of-flight secondary ion mass spectrometry

This page is intentionally left blank

SPENT FUEL AND WASTE SCIENCE AND TECHNOLOGY

FY18 STATUS REPORT: SNL RESEARCH INTO STRESS CORROSION CRACKING OF SNF INTERIM STORAGE CANISTERS

1 INTRODUCTION

This progress report describes work being done at Sandia National Laboratories (SNL) to assess the localized corrosion performance of container materials used in the interim storage of spent nuclear fuel (SNF). Of particular concern is stress corrosion cracking (SCC), a mechanism by which a through-wall crack could potentially form in a storage canister over time intervals that are shorter than possible dry storage times. Developing an understanding of stress corrosion cracking (SCC) of interim storage containers has been indicated as a high priority data gap by the Department of Energy (DOE) (Hanson et al., 2012), the Electric Power Research Institute (EPRI, 2011), the Nuclear Waste Technical Review Board (NWTRB, 2010), and the Nuclear Regulatory Commission (NRC, 2012; NRC, 2014).

1.1 Background

In dry storage SNF is commonly stored in welded stainless steel canisters enclosed in passively-ventilated overpacks. As outside air advects through the overpacks, dust accumulates on the canister surfaces. Over time, as the SNF cools, the canister surface temperatures drop to the point that salts within that dust will deliquesce to form concentrated brines. If the salts contain aggressive species such as chloride, then the resulting brine can cause localized corrosion—pitting—to occur. If sufficient stresses are present, the pitting can eventually convert to SCC, which over time, could penetrate the canister wall. The risk of corrosion and SCC is greatest in near-marine settings, where chloride-rich sea-salt aerosols are deposited on the canister surface.

A timeline for SCC of spent nuclear fuel canisters in dry storage is shown in Figure 1. Several important events and processes occur during the development of through-wall SCC, and understanding the timing of event initiation, and rate of processes, is critical to accurate evaluation of SCC penetration rates. These parameters are highly dependent upon the evolving physical and chemical environment on the canister surface, and on the canister material properties, including composition, surface finish, and weld-related microstructure and residual stress levels. SNL and several collaborators are working to understand these dependencies, and their effect on potential canister penetration rates by SCC. This information is critical to understanding the potential risk of canister failure during extended interim storage at reactor sites or at consolidated interim storage sites.

Immediately after placement into an overpack, canister surface temperatures are too high to permit salt deliquescence or even development of adsorbed water layers on salts, and localized corrosion cannot occur. Even after deliquescence, corrosion may be delayed for a time, although this period is likely to be insignificant relative to storage time intervals. This initial period is known as the incubation period, and is a function of the physical environment—the temperature, relative humidity (RH) and salt load on the canister surface. The chemical composition of the salt is also important, as it controls the RH at which deliquescence occurs. SNL is evaluating the physical conditions and the chemical environment on the canister surface, both prior to and after initiation of corrosion. Of particular interest is the long-term stability of brines formed by sea-salt deliquescence on the heated canister surface, and the effect of atmospheric exchange reactions and corrosion reactions.

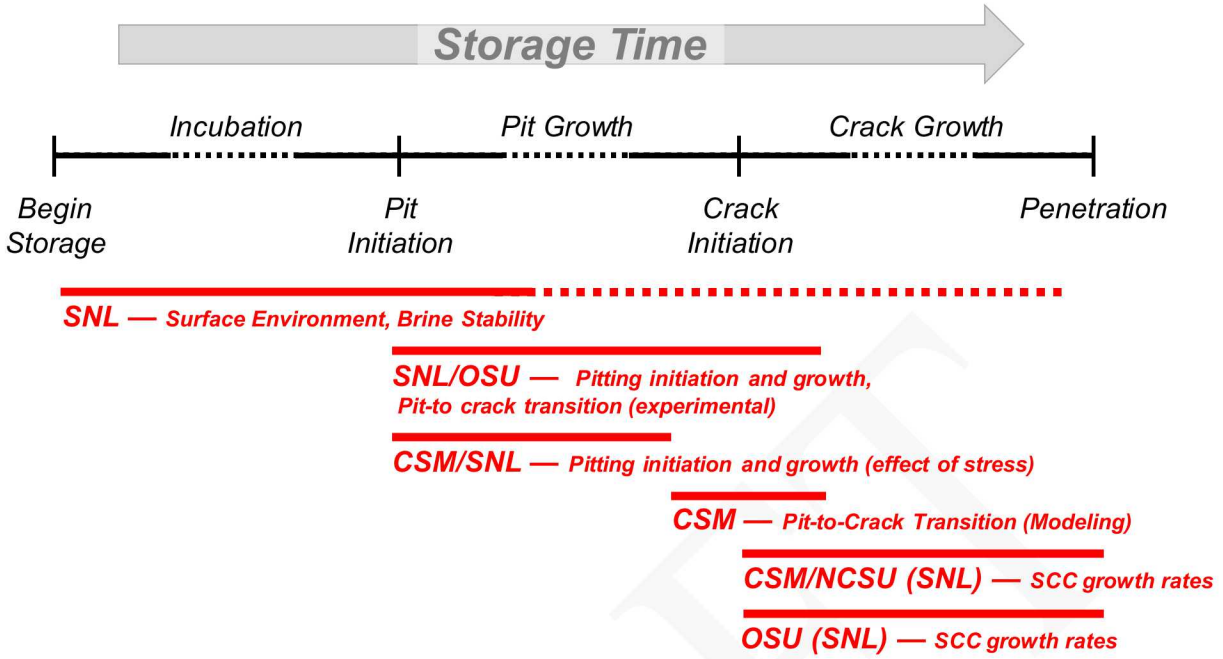

Figure 1. Timeline for stress corrosion cracking, showing current experimental work being carried out by SNL and collaborators.

Once deliquescence occurs, if the deliquescent brine is chemically aggressive (e.g. chloride-rich), then pitting corrosion will initiate. Pitting initiation and pit growth rates, and possible limitations on pit growth, are strongly controlled by environmental factors such as temperature, RH, and salt load, but also by material properties, including composition, surface finish, microstructure, and stress level. SNL is collaborating with the Colorado School of Mines (CSM) as part of a DOE Integrated Research Project (IRP) to evaluate the effect of stress on pit growth rates, and is working with Ohio State University (OSU) to evaluate pit initiation and growth on unstrained samples with different surface finishes. Collaboration with OSU is through their WastePD Energy Frontier Research Center (EFRC). SNL is also evaluating the effect of brine composition on cathodic reaction rates in region surrounding the pit, and also how those rates may change as corrosion reactions could affect the composition of the brine in the cathode region. This work is being carried out in collaboration with the University of Virginia.

In the presence of tensile stresses, the current assumption is that pits that grow sufficiently large will eventually initiate SCC cracks. Existing models relate pit depth to crack initiation through the calculated crack tip stress intensity factor (e.g., Kondo, 1989; Turnbull et al., 2006). However, this approach must be implemented stochastically, and makes broad assumptions about the shape of the pit. To develop a more realistic relationship between pitting and crack initiation, SNL is working with OSU to experimentally evaluate conditions of pit-to-crack transition under controlled conditions. SNL is also evaluating pitting and crack initiation using a large weld sample from a full-diameter canister mockup that SNL has previously used to characterize weld residual stresses (Enos and Bryan, 2016a).

Finally, once a SCC crack initiates, the rate of crack growth will be controlled by the temperature and chemical environment, as well as, possibly, the salt surface load. The overall level of tensile stress is also important, combining with the depth of the crack to determine the crack tip stress intensity factor (Newman and Raju, 1979; Newman and Raju, 1981). SNL is working with colleagues at North Carolina State University as part of the CSM-led IRP to measure crack growth rates as a function of brine composition. Finally, SNL is collaborating with OSU to evaluate the effect of salt load on crack growth rates—to determine if the limited cathode areas associated with thin brine films limit crack growth rates or crack depth. For crack growth testing, SNL's role to date has been to help define testing conditions;

and supporting post-test characterization of the SCC cracks that form in the tests. In FY19, we will actively begin to perform experimental work to assess environmental controls on crack growth rates.

1.2 FY18 Tasks and Current Status

Prediction of SCC formation initiation and growth requires both (a) a statistical description of the inherently stochastic process of pit formation, growth and conversion to a SCC crack under conditions (material and surface environment) representative of fielded canisters and (b) a deterministic/mechanistic understanding of environment-material-electrochemical interrelationships. Purely statistical approaches provide a means of quantifying variability and uncertainty in material and surface condition, but cannot be confidently extrapolated beyond the range of conditions or the time interval under which the data were collected, without a mechanistic understanding of the processes involved. Mechanistic studies serve to inform and provide confidence in statistical extrapolation for prediction of these processes. Sandia, the IRP and other collaborators are pursuing both avenues for prediction of SCC behavior of used fuel nuclear waste containers at independent spent fuel storage installation (ISFSI) sites. Challenges common to both approaches are lack of data on canister surface environment, and an incomplete understanding of the relationships between environment, material, and corrosion response under field-relevant conditions. This challenge manifests itself in selection of appropriate environmental and material inputs for models, development of experiments relating environment/material to damage rates and distributions, and utilization of experimental data as inputs and benchmarking tools for predictive models.

Efforts at SNL take advantage of unique combination of expertise and capabilities in geochemistry, surface science, metallurgy and electrochemistry to:

- Advance the quantitative definition of the physical and chemical environment on the surface of SNF interim storage canisters, and its temporal and spatial evolution to inform modeling and relevant laboratory experiments.
- Rigorously characterize the relationship between the surface environment and damage distributions and rates, with emphasis on electrochemical kinetics.
- Quantify the impact of materials variability (stress, strain, microstructure, surface finish) on electrochemical corrosion processes from pitting initiation to stress corrosion cracking.
- Quantify the effect of environmental controls (temperature, RH salt composition and load), and the evolution of brine properties on stress corrosion crack growth rates.

These efforts will provide knowledge and data necessary for relating canister-relevant surface environments and material conditions to corrosion processes. This understanding will support efforts at SNL and elsewhere to design and carry out relevant laboratory corrosion/SCC tests and to interpret the results of those tests. Ultimately, it will support improved modeling of storage canister performance during long-term interim storage.

Sandia research will focus on the thrust areas listed above. Testing will be done at experimental conditions (e.g., salt loading, humidity, temperature) that bound expected canister surface conditions in marine coastal environments, which are expected to be the most severe case for SCC.

2 CHARACTERIZATION OF THE CHEMICAL AND PHYSICAL ENVIRONMENT ON STORAGE CANISTER SURFACES

2.1 Magnesium Chloride Brine Stability

In most published experimental studies on sea-salt induced atmospheric corrosion, the experimental results are interpreted with the assumption that the salts deposited on the metal surface are sea-salts in composition, and that they, and the brines they form via deliquescence, do not change with exposure time, even after corrosion begins to occur. This is incorrect, as exchange reactions with the atmosphere and corrosion reactions modify the composition of the salts and brines. Understanding these processes is important, not only because it is required for proper interpretation of experimental results, but also because these reactions will occur in the field, affecting salt and brine compositions, and potentially limiting conditions under which corrosion can initiate, or once corrosion begins, limiting the extent of corrosion. Sandia's work in this area has focused of the stability of magnesium chloride brines, because those are the brines that would form first as the canister cools and the surface RH rises, and deposited sea-salt aerosols deliquesce. Previously (FY17), we evaluated potential carbonation of magnesium chloride brine, represented by (Schindelholz et al., 2017):

$$Mg^{+2}(aq) + 2Cl^{-}(aq) + H_2O + CO_2(g) \rightarrow MgCO_3(s) + 2HCl(g)$$

For simplicity, $MgCO_3$ (magnesite) is shown above, but this is just a placeholder. Magnesite itself is kinetically inhibited from precipitating, and a different Mg-carbonate, such as hydromagnesite ($Mg_5(CO_3)_4(OH)_2{:}4H_2O$) is frequently observed experimentally (Sayles and Fyfe, 1973; dos Anjos et al., 2011; Montes-Hernandez et al., 2012). There are many magnesium carbonate minerals with different CO_3:OH ratios and numbers of waters of hydration, and even a Mg-chloride-carbonate phase is known to exist.

When HCl(g) is degassed, the brine pH rises, causing the HCl(g) partial pressure being generated by the brine to decrease. However, the pH is partially buffered by absorption of CO_2 from the atmosphere and formation of carbonic acid. The carbonate concentration in the brine increases as HCl degassing continues, and the brine eventually saturates with magnesium carbonate, which begins to precipitate out. At this point, the pH is fully buffered, and the brine composition becomes invariant; further degassing continues without affecting the pH or the HCl partial pressure; the brine can fully convert to carbonate. This will occur if the HCl partial pressure being generated at the point of carbonate precipitation exceeds the HCl partial pressure in the environment. The brines that are predicted to form by sea-salt deliquescence are in equilibrium with the atmospheric CO_2 levels, and are already saturated with a magnesium carbonate (Schindelholz et al., 2017)—HCl degassing has no effect on the brine composition, but results in conversion of $MgCl_2$ to carbonate and dry-out of the brine. As noted previously, magnesite is assumed to be kinetically inhibited, and hydromagnesite precipitates; if magnesite does form, then the pH will be lower at the point of carbonate precipitation and the HCl partial pressure higher.

To evaluate this thermodynamically, the thermodynamic solubility and speciation modeling program EQ3/6 (Wolery and Jarek, 2003) and the YMP Pitzer database (SNL, 2007) were used. We assume that this reaction can occur as soon as deliquescence occurs (or even before, if a water film forms on the salt surface below the deliquescence RH); therefore Mg^{+2} and Cl^{-} concentrations were fixed to be at saturation with $MgCl_2{:}6H_2O$ (bischofite) at the temperature of interest; this also determines the H_2O activity. The CO_2 gas concentration was set to the current atmospheric value of $10^{-3.4}$ bars. The HCl partial pressure generated by the brine is strongly controlled by the temperature. Therefore, Mg-carbonate and $MgCl_2{:}6H_2O$ (bischofite) stability fields were determined as a function of canister surface temperature and atmospheric HCl(g) concentration. The results are shown in Figure 2; also shown are typical ranges for atmospheric HCl concentrations in marine, continental, and industrial settings (Vierkorn-Rudolph et al., 1984; Möller, 1990; Harris et al., 1992; Kulmala et al., 1998; Crisp et al., 2014).

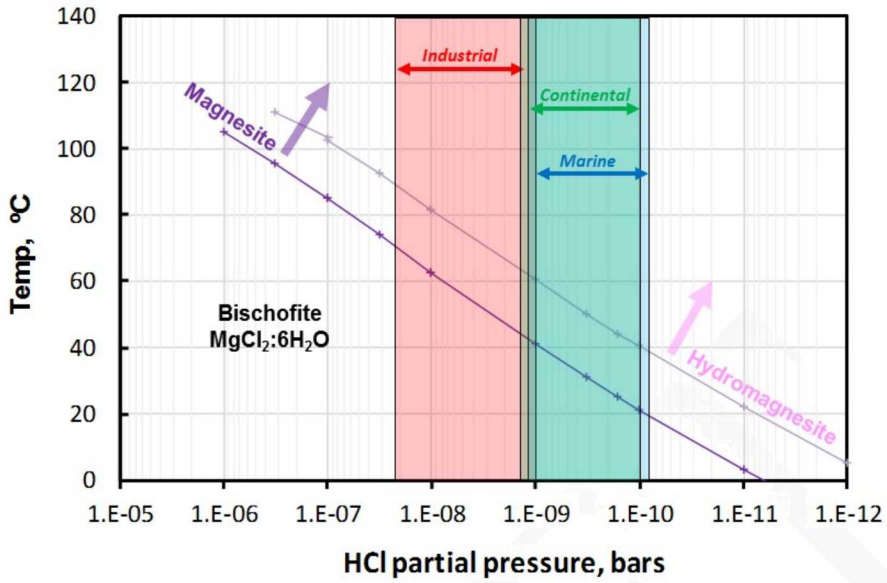

Figure 2. Stability fields for bischofite, magnesite, and hydromagnesite, as a function of temperature and HCl partial pressure.

In FY17, we experimentally evaluated the extent of this reaction at 48°C and 40%RH, conditions under which the magnesium chloride should be deliquesced, by depositing droplets of magnesium chloride brine onto silicon wafers and then ageing the wafers in an RH chamber for up to 69 days (Schindelholz et al., 2017). Air flow was maintained through the chamber at a flow rate of 2L/ using air that had been passed through a "Zero Air" system capable of removing all contaminants (organic compounds and acid gases) from the air stream. CO_2 was not removed by the Zero-Air system. Hence, in Figure 2, conditions would be far to the right of the bischofite stability field, and a magnesium carbonate should be stable. After 69 days, the wafers were removed from the RH chamber and examined by scanning electron microscopy/energy dispersive spectroscopy (SEM/EDS), and by chemical analysis. The results indicated that the magnesium chloride had partially converted to magnesium carbonate (Figure 3, Figure 4). Only some of the deposited droplets converted, and even they were not fully converted; in Figure 3, the converted droplets exhibited a different morphology, reduced chloride concentrations, and enrichments in carbon. Smaller droplets (<10µm in diameter) preferentially reacted, possibly because of higher surface-area-to-volume ratios. The degassing process was slow; following exposure and SEM analysis, the salts were washed off the silicon wafer and analyzed by ion chromatography (IC). The percent chloride lost for the two 69-day samples, was 13% to 21% (Figure 4); low salt loads made accurate analysis difficult.

Only partial conversion was anticipated, however. At the HCl partial pressures predicted by the thermodynamic calculations (Figure 2) each cubic meter of air passing through the humidity chamber could only remove ~0.4 µg (hydromagnesite-buffered) to ~3 µg (magnesite-buffered) of chloride, assuming complete equilibration between brine and atmosphere. At the gas flow rate used (2 L/min) and the measured salt loadings (65.6 —g/sample), a single sample would take 15 days (magnesite) to 112 days (hydromagnesite) to fully degas. With six samples in the chamber for the first 30 days and three samples for the next 38 days, full degassing was not possible, even if complete equilibration between the headspace gas and the deposited samples had occurred. No such limitation is present for magnesium chloride on a canister surface, because airflow through overpacks is on the order of cubic meters per minute, based on computational fluid dynamics calculations of heat-driven advection through the systems (Suffield et al., 2012). The main conclusion of the FY 17 experiments was that HCl degassing does occur from $MgCl_2$ brines, and does result in chloride loss, carbonation, and potentially, brine dryout.

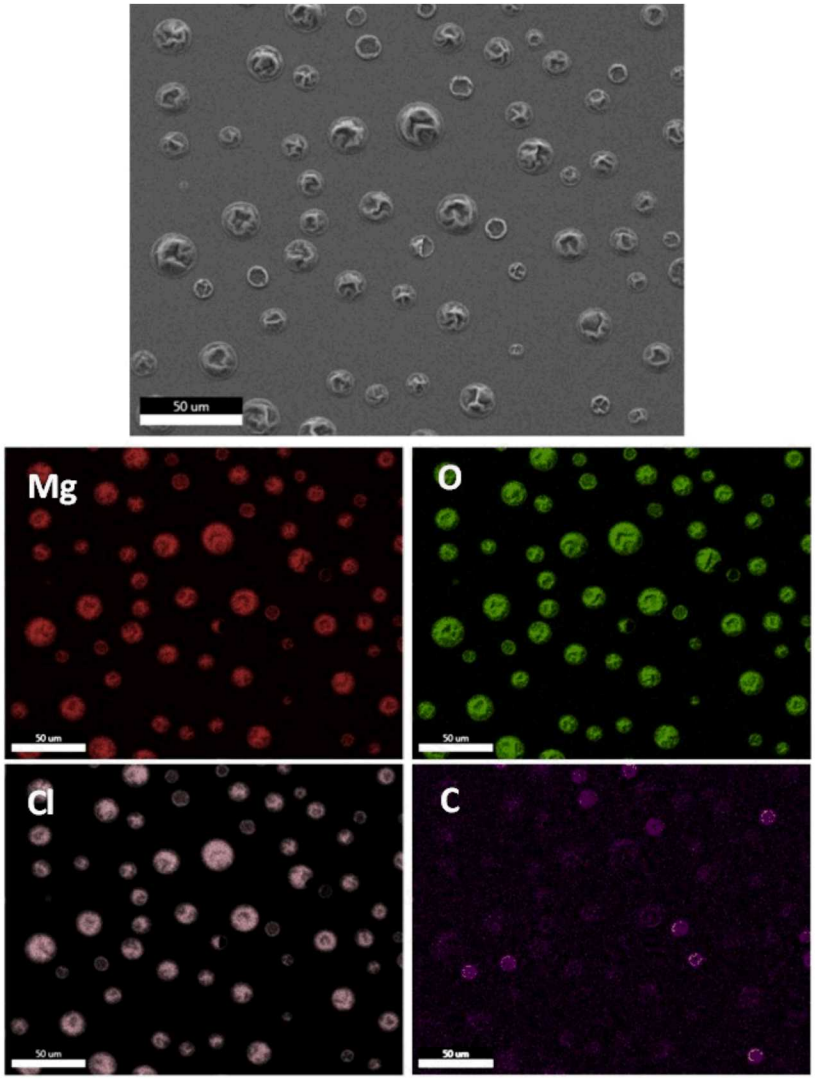

Figure 3. Element map of dried magnesium chloride brine droplets exposed for 69 days at 48°C and 40%RH.

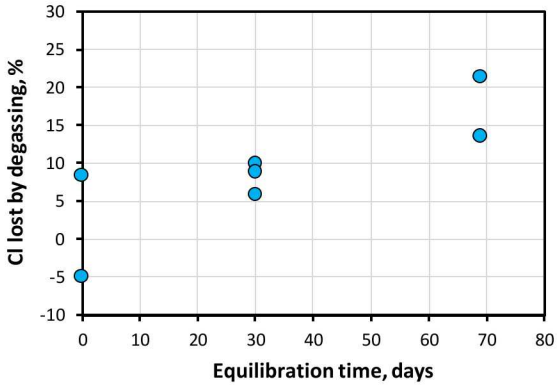

Figure 4. Fraction of chloride lost, as a function of equilibration time.

2.1.1 FY18 Magnesium chloride degassing experiment

In FY 18, we have evaluated magnesium chloride brine stability under a different set of conditions, at 80°C and 35% RH. These conditions were chosen for three reasons. First, higher temperatures result in the brine generating higher partial pressures of HCl, leading to higher degassing rates. The partial pressure of HCl over a magnesium chloride brine in equilibrium with magnesium carbonate is equivalent to 11 $\mu g/m^3$ (hydromagnesite) and 83 $\mu g/m^3$ (bischofite), resulting in more rapid conversion to carbonate. Second, these conditions are consistent with those use in experiments by the Japanese Central Research Institute of the Electric Power Industry (CRIEPI) to evaluate SCC crack growth rates, and the results of these experiments may clarify the interpretation of the Japanese experiments. Finally, we are currently carrying out corrosion experiments with large plates of the Sandia full diameter canister mockup (see Section 4) under similar conditions—magnesium chloride brine at 80ºC and 35% RH—and this experiment, evaluating $MgCl_2$ brines deposited on an inert matrix, will potentially aid with interpretation of the corrosion experiments with stainless steel.

The experimental design was largely the same as that used previously (Schindelholz et al., 2017). Magnesium chloride brine (1M, in 17% ethanol solution) was sprayed onto an inert substrate—polished silicon wafers 25 mm in diameter—using an ink-jet printer as described in Schindelholz and Kelly (2010a). This deposition method produced randomly-spaced, isolated droplets of brine on the wafer surface. A much higher salt load was used in this experiment to make chemical quantification easier, and droplet coalescence resulted in a much larger droplet size range than in the previous experiment. Droplets varied from 10 to 150 microns in diameter, as shown in a SEM backscattered electron (BSE) image of the deposited salts (Figure 5). The initial salt load was about 300 $\mu g/cm^2$ $MgCl_2$:$6H_2O$ (1520 µg/sample), or 105 $\mu g/cm^2$ Cl (530 µg/sample).

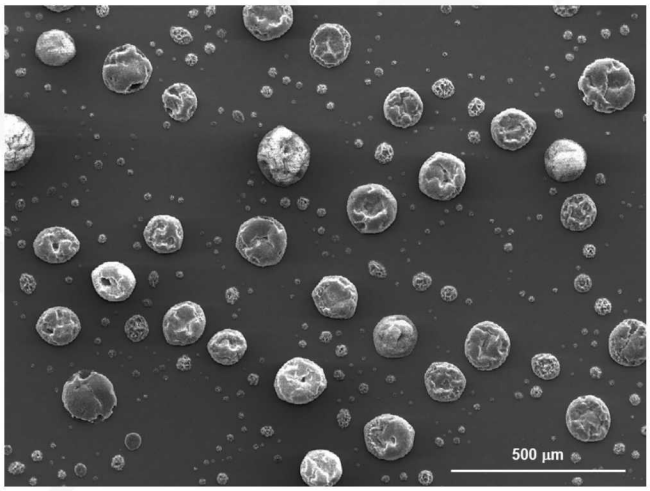

Figure 5. SEM BSE image of the $MgCl_2$ droplets deposited on a silicon wafer, showing the range of droplet sizes present.

After salt deposition, the wafers were stored in a nitrogen purged cabinet until use. Three samples were retained to quantify the initial condition, and the remaining nine samples were placed in a controlled-humidity chamber at 80º C and 35% RH, slightly above the deliquescence RH of $MgCl_2$:$6H_2O$. The atmosphere in the chamber was replaced at a rate of 2 L/min, using air that had been passed through the "Zero-air" system described previously. Three samples pulled after 14 days, three more after 28 days, and the final three, along with a blank wafer as a control, after 56 days. All samples were stored in a cabinet purged with dry nitrogen until analysis.

In order to determine whether HCl degassing occurred, the samples are being analyzed in several ways. Selected samples from each sampling episode were analyzed by SEM/EDS, and the 56-day samples were analyzed by X-ray diffraction (XRD). As discussed below, initial results suggest that significant degassing occurred, and further analyses will verify this and quantify the degree of degassing. Micro-Fourier Transform Infrared (FTIR) Spectroscopy and micro-Raman spectroscopy will provide information on the secondary phases that form, and are in the process of being carried out. Grazing incidence angle XRD may provide better X-ray diffraction data, and Time-of-Flight Secondary Ion Mass Spectrometry (TOF-SIMS) will provide compositional data. Finally, all samples will be leached with deionized water, and the dissolved salts were analyzed by IC. This does not provide information on carbonate, but does give Mg and Cl concentrations, and degree of chloride loss by degassing.

2-week samples

Only one of the samples collected after two weeks of exposure was examined by SEM/EDS. SEM secondary electron (SE) images of the sample are shown in Figure 6. After two weeks, many of the smaller droplets appeared to have lost most of their volume and developed into highly porous masses of fibrous, hairlike crystals. Conversely, the larger droplets mostly retaining a smooth hemispherical outer surface, although some developed a fine hairlike coating, similar to the texture of the smaller droplets. The differences in texture suggest potential variations in mineralogy, and EDS analysis was carried out to see if there were any compositional differences. The only major difference in the X-ray spectra between larger and smaller droplets was that the X-ray peak for Si was larger for the smaller droplets, as the electron beam interaction volume included more of the Si substrate. Mg/Cl integrated peak area ratios for all EDS analyses collected from the sample are provided in Figure 8. For many reasons, EDS peak areas do not correspond directly to elemental concentrations; however, they do provide qualitative evidence of changes in relative elemental concentrations. The Mg/Cl ratios vary only slightly with droplet size, with smaller droplets showing a slightly higher Mg/Cl value. Given the uncertainty in effects of the geometry (thin films deposited on a silicon substrate) on possible secondary fluorescence of magnesium vs. chloride, it is difficult to place much weight in the small differences observed.

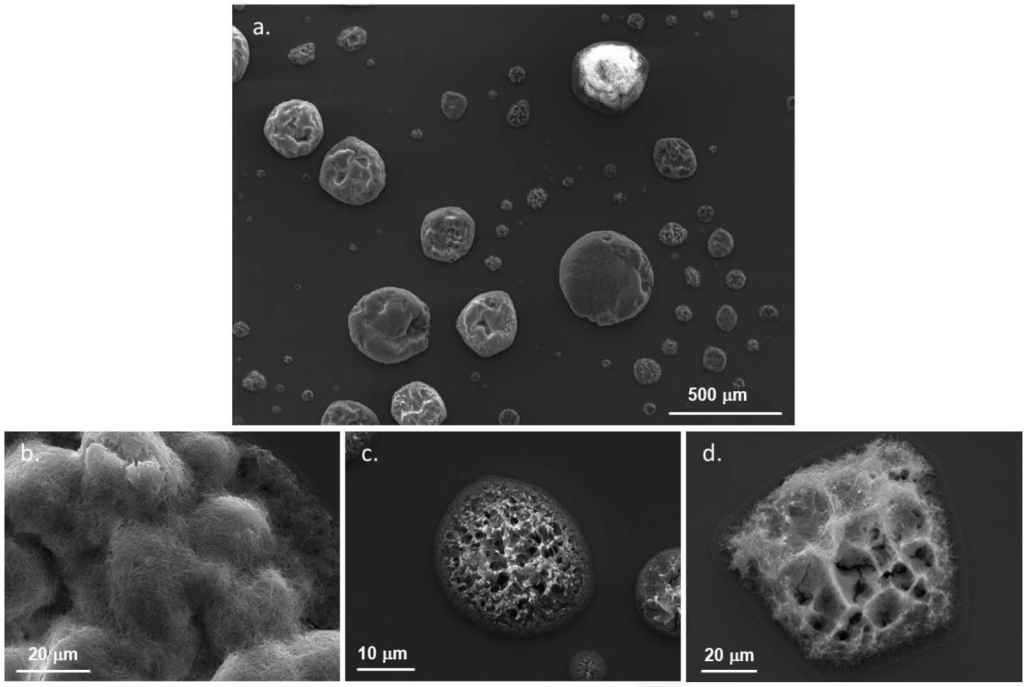

Figure 6. SEM images of $MgCl_2$ sample, exposed for 2 weeks, showing variations in texture with droplet size. a) Low magnification view, showing all droplets; b) magnified view of rare droplet with fibrous outer layer; c) and d), magnified views of small droplets, showing fibrous texture.

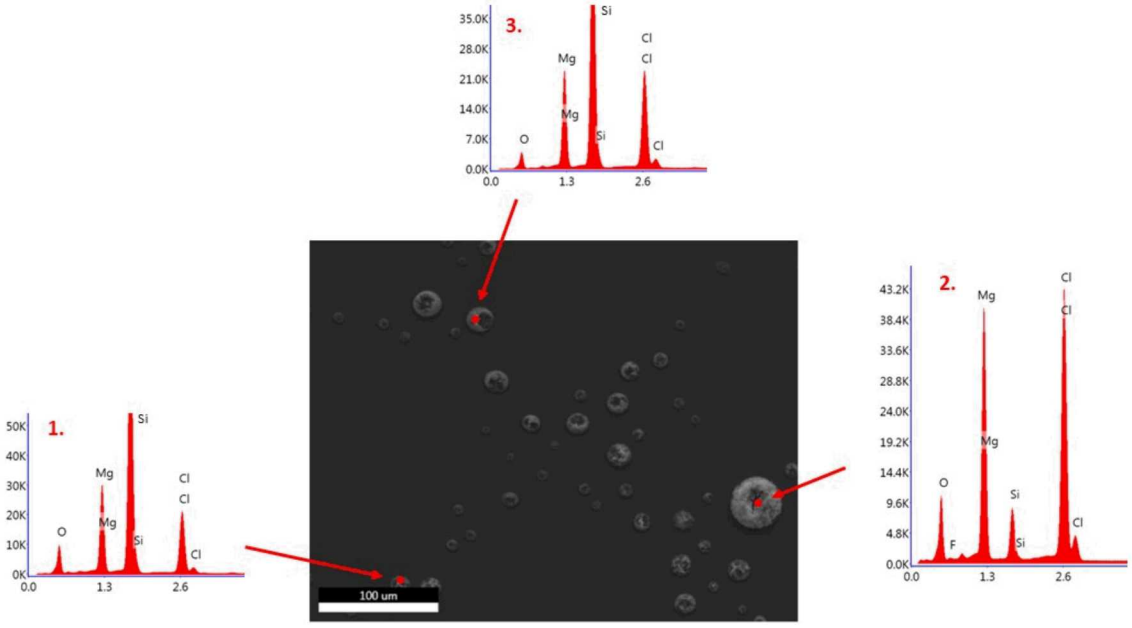

Figure 7. EDS analyses of individual droplets, 2-week sample

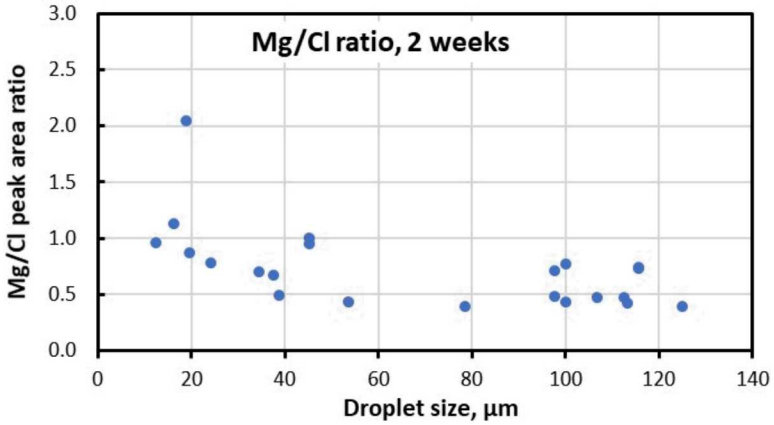

Figure 8. Mg/Cl peak area ratios as a function of droplet size, for the 2-week sample.

4-week samples

Only one of the samples collected after four weeks of exposure was examined by SEM/EDS. SEM backscattered electron (BSE) images of the sample are shown in Figure 9. The large droplets no longer look smooth, but developed (presumably upon removal from the RH chamber and drying), a crystalline texture, or at least a crystalline outer shell. In the area imaged in Figure 9, there is little variation in droplet brightness with size, suggesting little compositional variation—in a BSE image, feature brightness is directly related to the average atomic number (z) of the material, with materials having a higher average z having a greater brightness. EDS analyses in this region showed that this was largely true. However, in other areas on the silicon wafer, as shown in Figure 10, there were notable differences in the brightness of the features, with the smaller droplets appearing as darker, indicating a lower average z. Because chlorine has the highest atomic number of the elements present (Cl-17, Mg-12, O-8, C-6, H-1), this suggests that the smaller droplets are depleted in chlorine. EDS analyses in this region confirmed that this was true, with Mg/Cl ratios varying significantly with droplet size (Figure 11). Mg/Cl ratios for all EDS analyses taken on this sample are provided in Figure 12, and clearly show that Mg/Cl ratios increase as the droplets get smaller. While previously the change in Mg/Cl ratio may have been a measurement artifact, the relative change now is much greater; in addition, had the trend simply been due to different droplet sizes and the resulting salt layer thicknesses on the silicon, there would have been no change with ageing time. These results suggest preferential chloride degassing from the smaller droplets, and are consistent with what was observed in FY17 experiments—smaller, higher surface area-to-mass droplets seem to preferentially react.

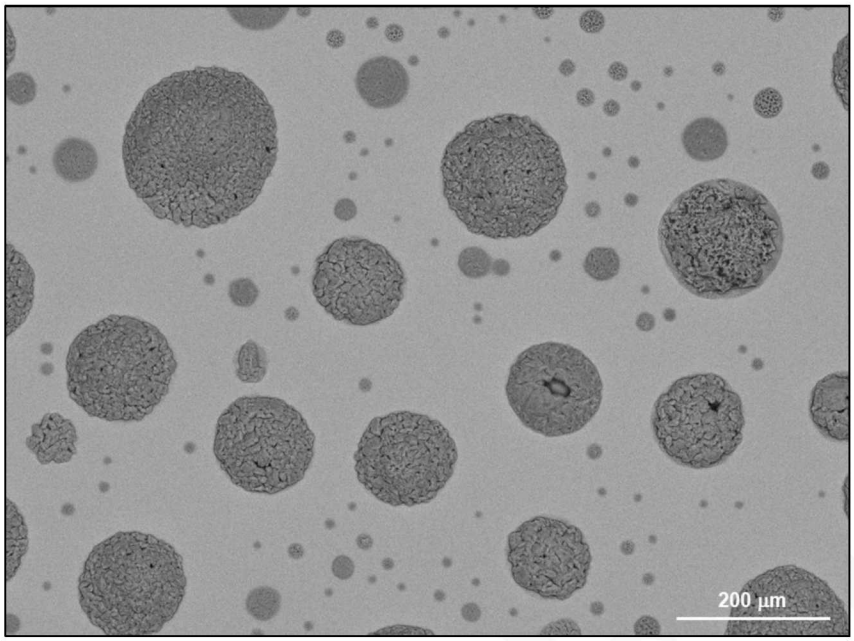

Figure 9. Low magnification BSE image of SEM images of 4-week $MgCl_2$ sample

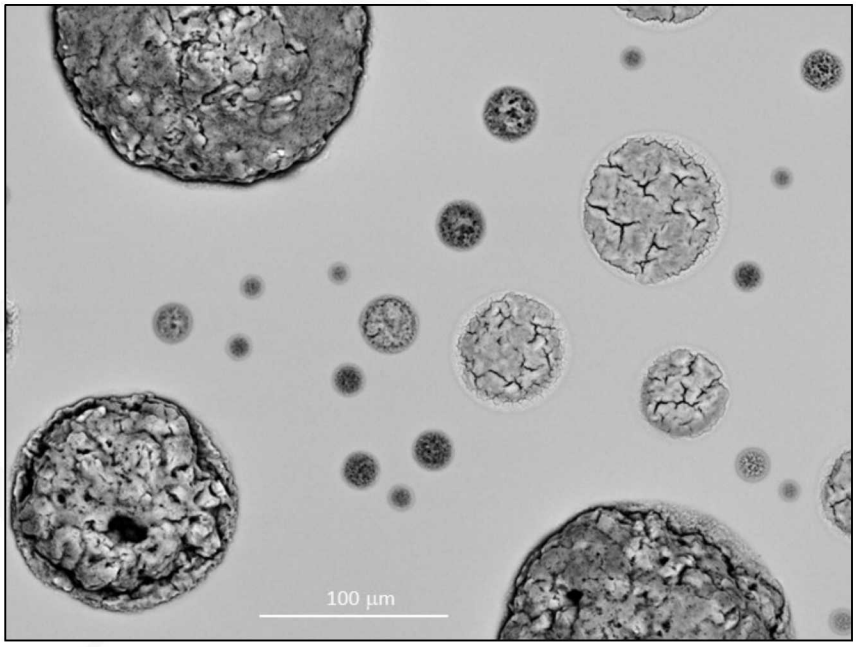

Figure 10. SEM BSE images of 4-week $MgCl_2$ sample, showing variations in brightness (average z) with droplet size.

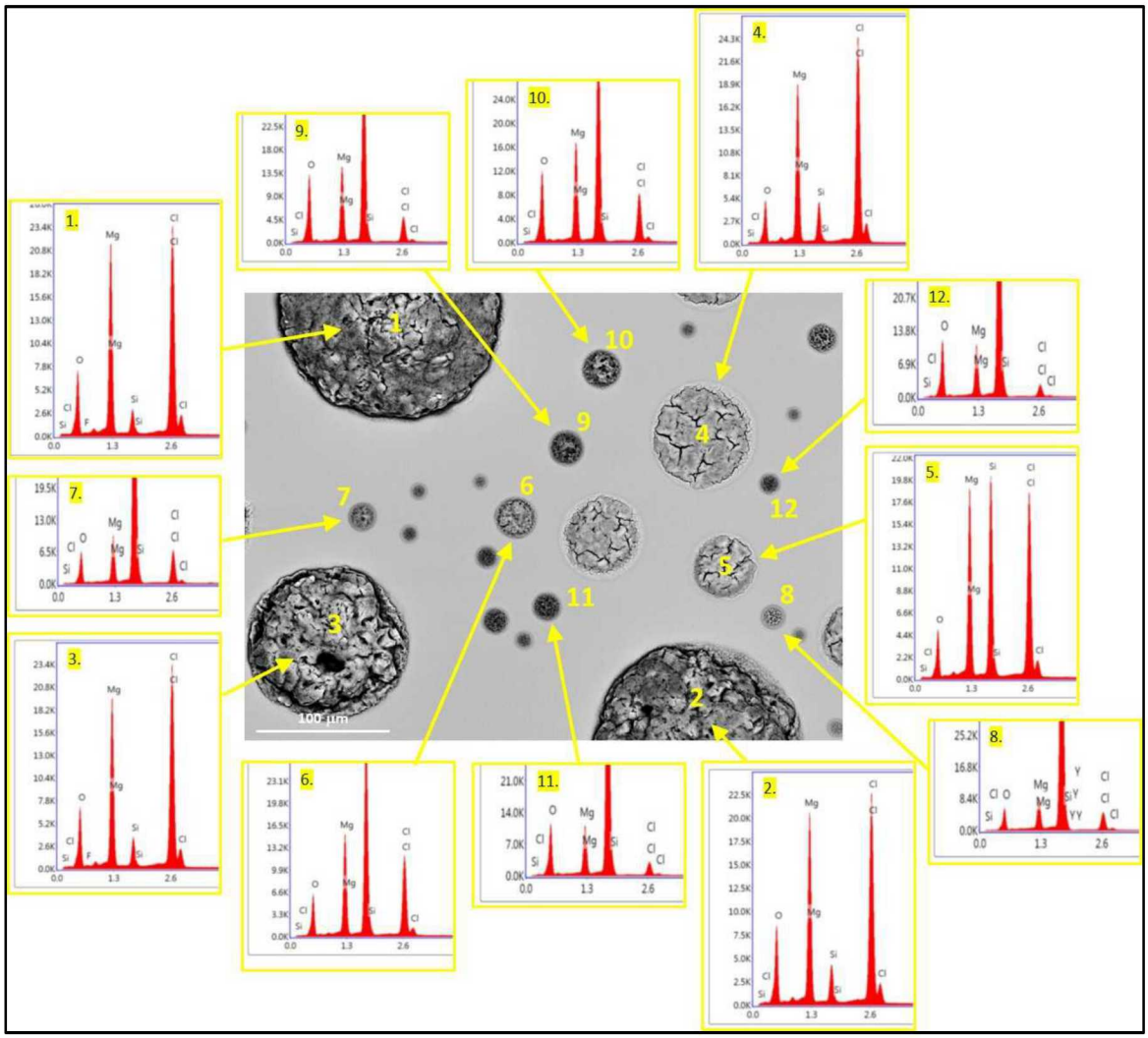

Figure 11. EDS analyses of different droplets, 4-week $MgCl_2$ sample, showing variations in composition with droplet size.

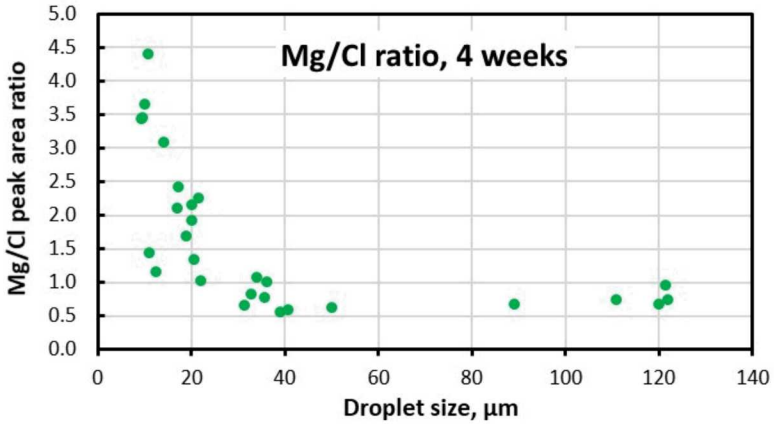

Figure 12. Mg/Cl peak area ratios as a function of droplet size, for the 4-week sample.

8-week samples

The three samples were collected after eight weeks of exposure, Samples #12, #14, and #19. Each was examined by SEM/EDS. There was considerable variability between the samples, and even from location to location on each sample, but in in all three cases, evidence of chloride loss was observed. Figure 13 is a BSE image and element maps of a particularly clear region on Sample #14. As with the 4-week sample that was examined there is a clear bimodality in the brightness of the droplets, and the element maps show that the brightness corresponds to compositional differences. Virtually all smaller droplets, and some large droplets, are depleted in chloride and relatively enriched in oxygen. A close-up of droplets within this area (Figure 14) shows that the smaller droplets appear to also be slightly enriched in carbon. EDS X-ray spectra of the droplets are shown in Figure 15. The spectra verify that droplet brightness directly corresponds to degree of chloride depletion and carbonate enrichment, but also shows droplet size alone is not an accurate discriminant of chloride depletion or carbonate absorption (compare droplets 5 and 2, for instance).

Mg/Cl ratios for all EDS analyses taken on Sample #14 are provided in Figure 16, and clearly show the general trend of an increase in Mg/Cl ratio as droplets get smaller—but also show that not all small droplets are depleted in Cl. The other two samples showed similar trends, although as stated previously, there was significant variability with location on each wafer.

Mg/Cl ratios for the 2-week, 4-week, and 8-week samples are shown in Figure 17. There is a clear progression over the course of the experiment. Only the smallest droplets show evidence of chloride loss after 2 weeks, but over time, the spectra of progressively larger droplets show chloride loss and smaller particles show an increasing degree of chloride loss. By 8 weeks, chloride loss appeared to level out for the smaller droplets, suggesting that they had completely converted to a different, non-deliquescent phase.

What phase formed? The amount of carbon present is insufficient for this to be a carbonate phase; although thermodynamically favored, it is likely that kinetic limitations, either in carbonate precipitation (magnesium carbonate is notoriously hard to precipitate), or in CO_2 absorption from the atmosphere, inhibited magnesium carbonate precipitation. This would allow the pH to rise to higher levels, eventually resulting in precipitation of a magnesium hydroxychloride hydrate.

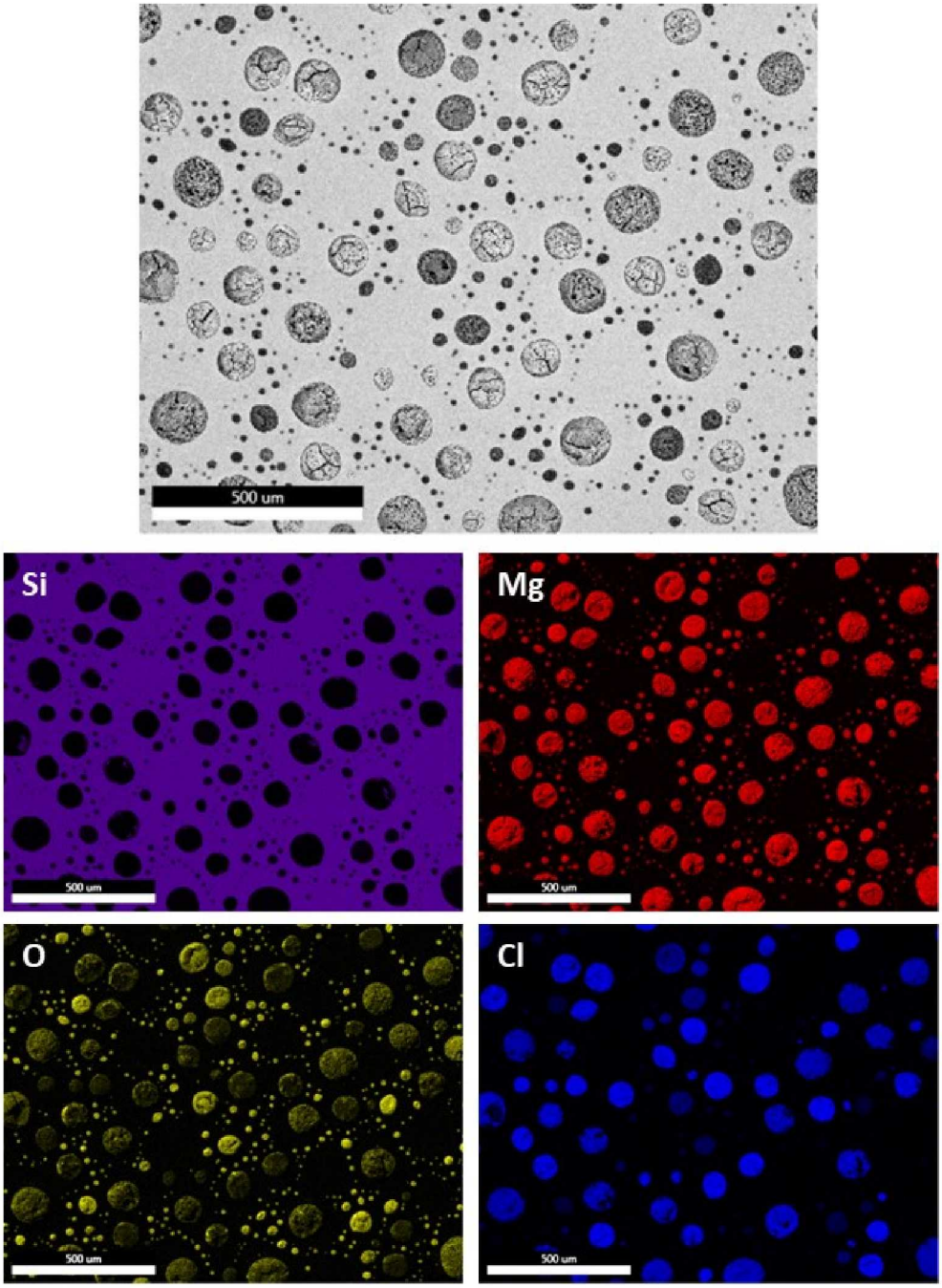

Figure 13. SEM BSE image and EDS element maps of 8-week $MgCl_2$ sample, showing variations in brightness (average z) with droplet size. Darker droplets are depleted in chloride and enriched in oxygen relative to brighter droplets.

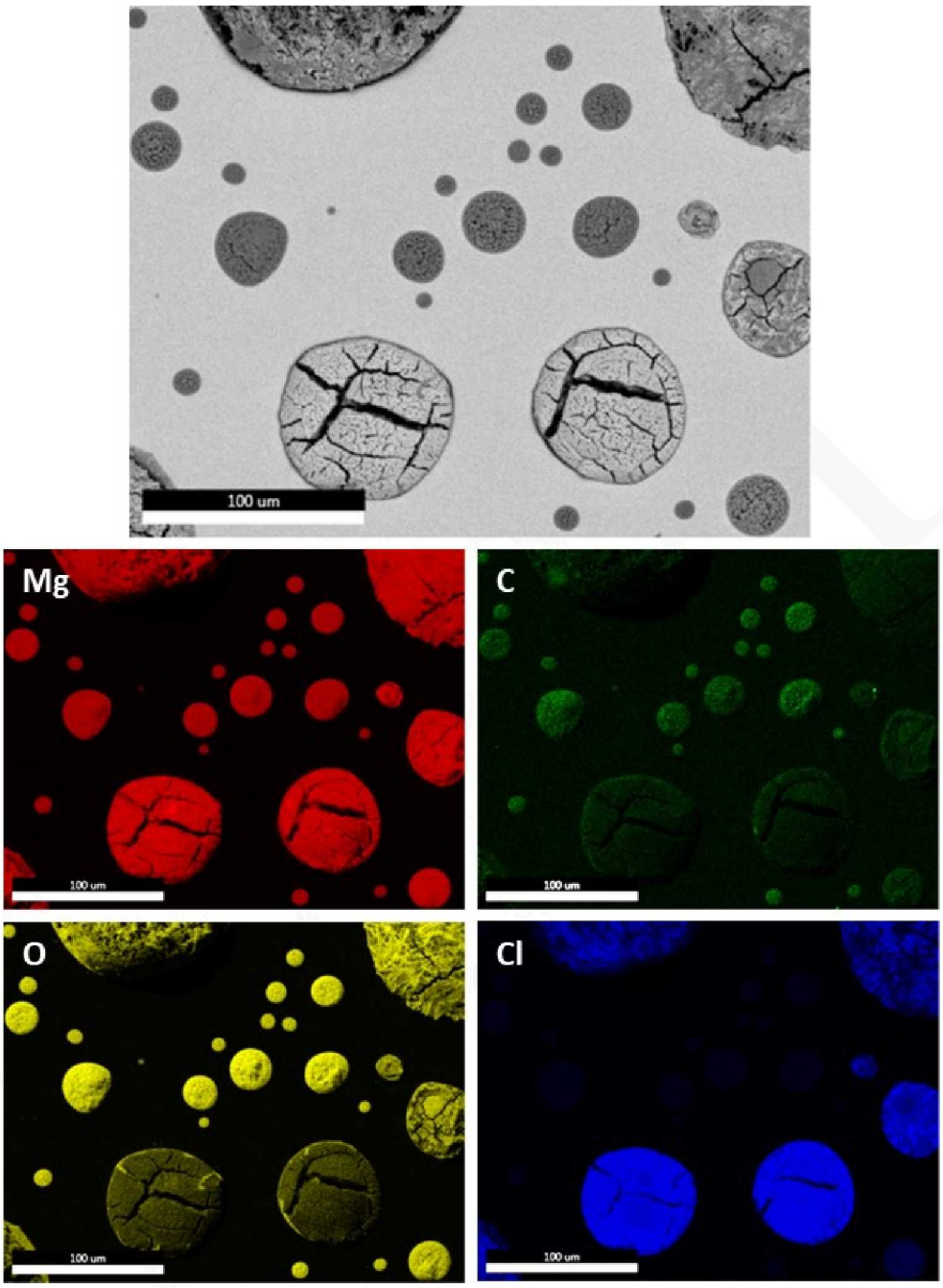

Figure 14. Higher magnification SEM BSE image and EDS element maps of 8-week $MgCl_2$ sample. Close-up element maps show that darker droplets, in addition to being depleted in chloride and enriched in oxygen, are enriched in carbon.

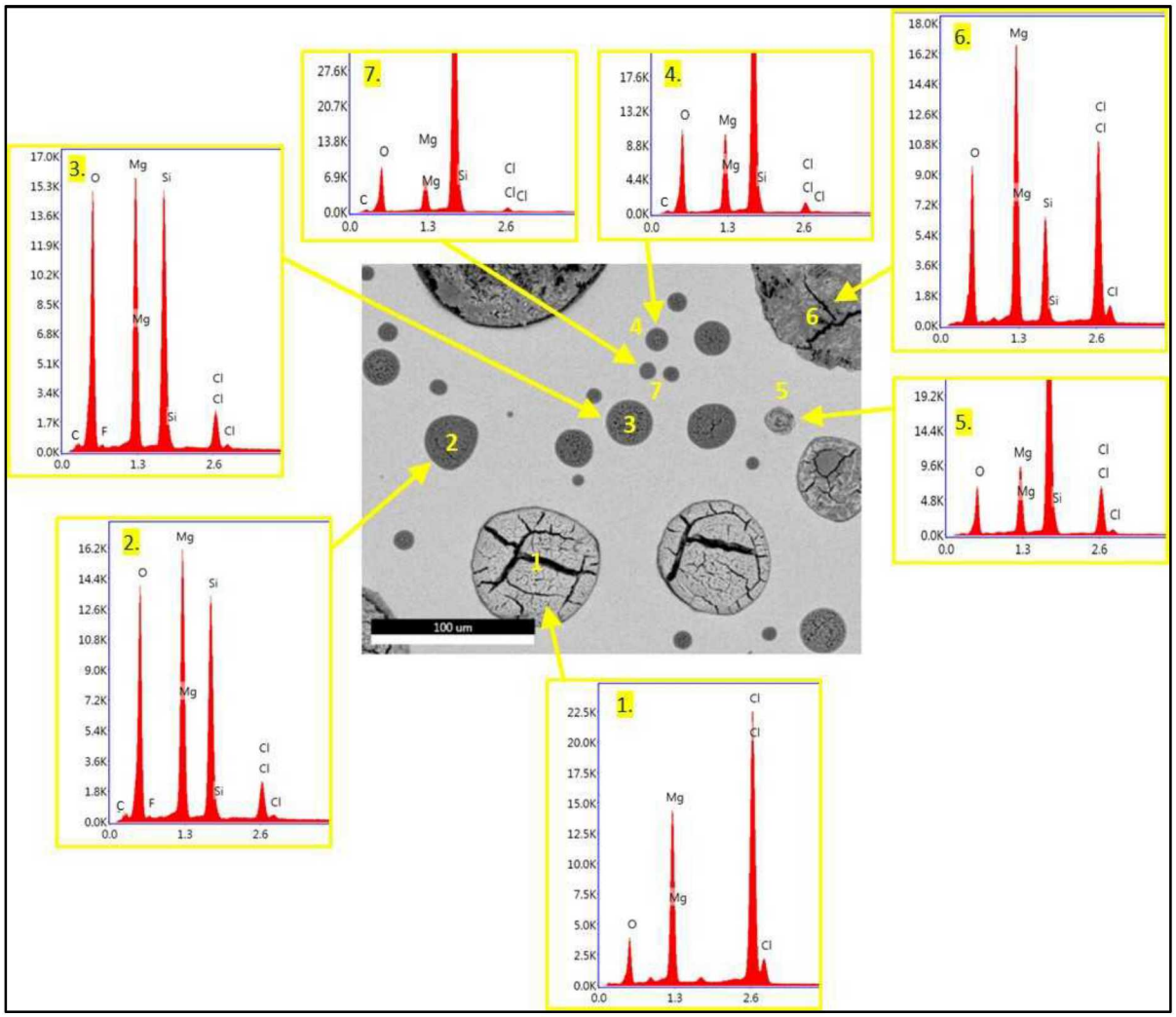

Figure 15. EDS analyses of individual droplets on the 8-week $MgCl_2$ sample, showing differences in composition with droplet size and brightness.

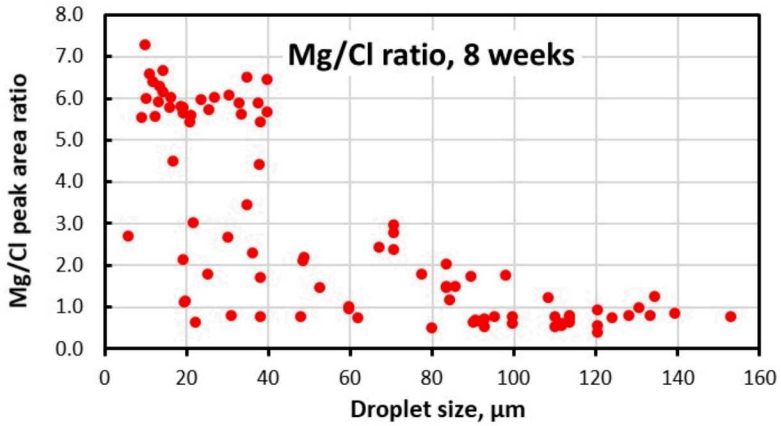

Figure 16. Mg/Cl peak area ratios for the 8-week $MgCl_2$ sample, showing strong dependence on droplet size.

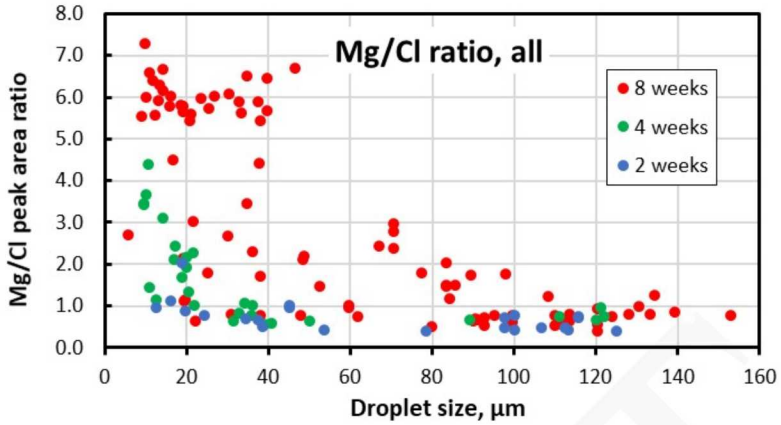

Figure 17. Comparison Mg/Cl peak area ratios for the 2-week, 4-week, and 8-week $MgCl_2$ samples.

Discussion

The identity of the precipitated phase cannot be determined by SEM/EDS. To evaluate the overall degree of conversion, and in an attempt to identify the precipitated phase, each of the 8-week samples was analyzed on the silicon wafer by X-ray diffraction (XRD) using a simple theta/2theta approach. The results are shown in Figure 18. The patterns are noisy, because the scans were carried out quickly in an attempt to avoid deliquescence—bischofite is highly deliquescent even when just exposed to room air. The patterns for two samples, #14 and #19, show only peaks for bischofite ($MgCl_2$:$6H_2O$); there is no visible second phase, indicating that if present, it could only constitute a small fraction of total material. The third sample, #12, deliquesced during sample preparation. The bischofite deliquesced, there are no characteristic peaks for that phase. However, a few small peaks were still present in the pattern (Figure 18), indicating the presence of a second phase. The peaks matched up with a magnesium hydroxychloride hydrate phase with the approximate composition of $(Mg(OH)_2)_2MgCl_2$:$4H_2O$, a phase that has been recognized to form in highly concentrated magnesium chloride brines at temperatures similar to those used here (de Bakker et al., 2012), although we cannot assess whether the relevant pH was present with the available data. The poor quality of the X-ray patterns makes the identification tentative; however, the identification is supported by the positive identification of the same phase as forming by conversion of magnesium chloride on the surface of corroding stainless steel under identical test conditions (temperature and RH). This is discussed in the next section.

A second important conclusion is that, since the hydroxychloride phase was still present when the bischofite had deliquesced, it must be less deliquescent. If exposed for a sufficiently long time at 80°C and 35% RH, a magnesium chloride brine will eventually convert completely to hydroxychloride and dry out.

In an additional analysis, a small amount of the salts from the silicon wafers was removed for each of the three 8-week samples, and transferred to carbon tape for analysis by SEM/EDS. This was done to verify that the silicon wafer had truly acted as an inert substrate, and had not reacted with brine to form magnesium silicate. The EDS analysis confirmed that no silicon was present in the salts.

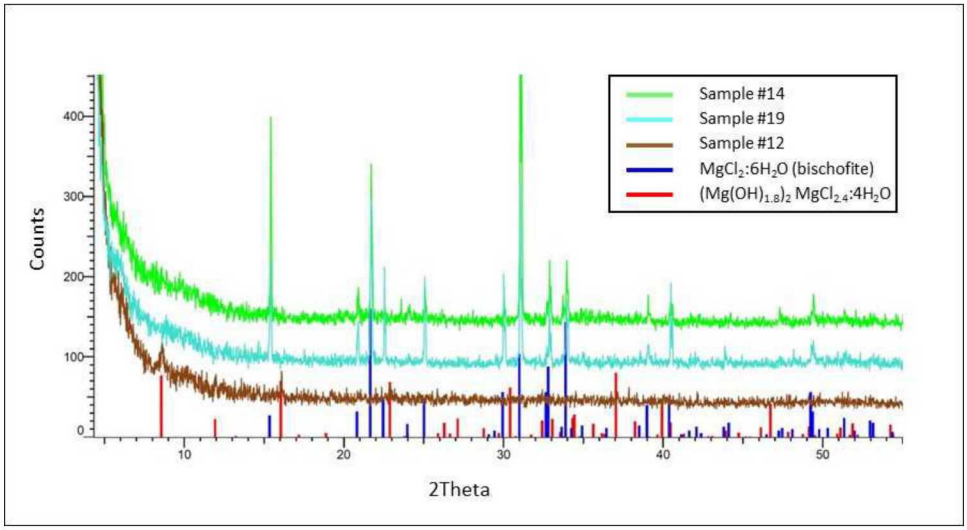

Figure 18. X-ray diffraction patterns for the three 8-week samples

Additional analyses are in progress. The samples are currently being analyzed by micro-FTIR and micro-Raman spectroscopy, techniques which able the detect changes in the composition of the magnesium chloride salt over time. The salt is initially bischofite ($MgCl_2$:$6H_2O$); conversion to carbonate or hydroxychloride would change the absorption spectra of the salts, allowing us to determine if such reactions have occurred. Time-of-flight secondary ion mass spectrometry (TOF-SIMS) microanalysis will potentially allow measurement of magnesium/chloride ratios directly, and determination of the composition of the secondary magnesium hydroxychloride phase that formed. Finally, glancing angle XRD will be attempted in an effort to obtain a better X-ray pattern for the hydroxychloride phase.

2.1.2 Magnesium chloride brine stability during metal corrosion

In the previous section, the stability of magnesium chloride brines and salts on an inert substrate was evaluated. This condition potentially applies to magnesium chloride in sea-salts prior to initiation of corrosion. However, following initiation of corrosion, chemical reactions may result in additional changes. Once corrosion initiates, brine compositions change both in the anode (the pit) and in the surrounding cathode. Anode solutions become highly acidic, because of metal hydrolysis reactions, while in the cathode, oxygen reduction results in the generation of hydroxyl groups, and an increase in pH. Several of these reactions could potentially limit the extent of corrosion by removing or sequestering the corrosive species, or by causing brine dry-out. Acidic conditions in the pit may support acid degassing, potentially resulting in chloride loss from the metal surface. The pH increases with increasing distance from the pit, and hydrolyzed metal ions can precipitate as chloride-containing corrosion products such as akaganeite, sequestering chloride from further reaction. In the cathode, high pH values can cause precipitation of hydroxides of carbonates (high pH solutions scavenge CO_2 from the atmosphere), potentially leading to brine dryout (Schaller et al., 2017).

In corrosion experiments that have been carried out over the last year, we have seen evidence that, at least under the conditions of the tests, magnesium chloride brine is not stable. In one experiment, a 4-point bend specimen was coated with salts and exposed to the same conditions as the brine stability experiments, 80°C and 35% RH. The tensile stress region (Figure 19) of the 4-inch wide beam was coated with four different salt loads: (1) 5 µL, 10 µL, and 20 µL droplets of saturated $MgCl_2$; (2) NaCl deposited as tiny isolate droplets with an inkjet; (3) sea-water, deposited as a pool with the same chloride load as the NaCl in quadrant 2; and (4) 5 µL, 10 µL, and 20 µL droplets of sea-water. Over two months in the RH chamber, all quadrants experienced corrosion (although it is likely that the NaCl quadrant

corroded while sitting on the benchtop after exposure and prior to cleaning). Upon removal from the oven, a white residue was observed surrounding the corroded zone in quadrant 1 (Figure 20). This material was carefully removed from the sample and analyzed by XRD and micro-Raman (Figure 21). The XRD pattern showed that two phases were present--bischofite, and $(Mg(OH)_2)_2MgCl_2{:}4H_2O$ (approximately), the same phase tentatively identified on the 8-week sample in the magnesium chloride brine stability experiment (Figure 18). The micro-Raman analysis also showed sharp hydroxyl peaks in the water region (3500-3700 wave-numbers) that are not present in bischofite.

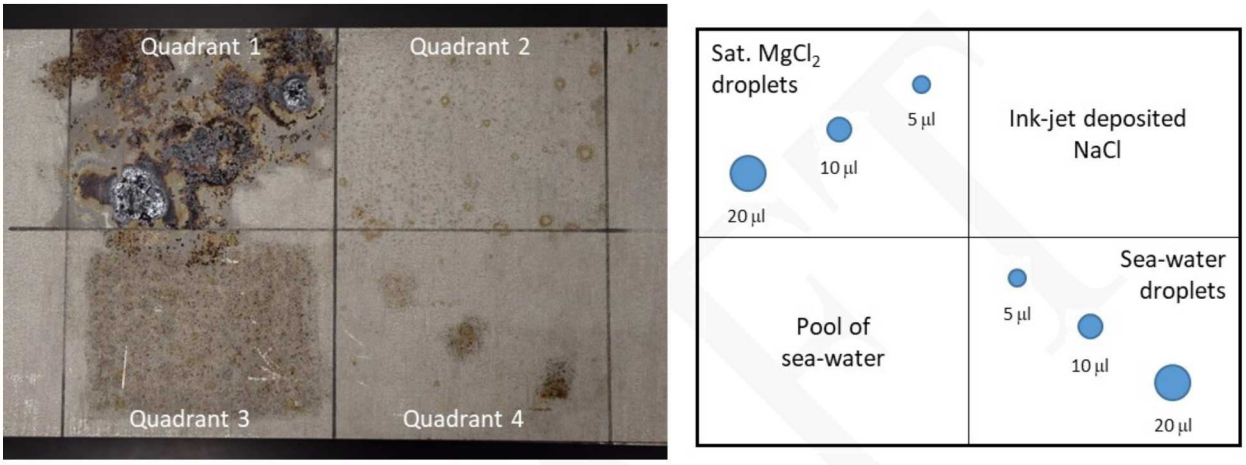

Figure 19. Salt deposition and corrosion of 4-point bend specimen exposed at 80ºC and 35% RH.

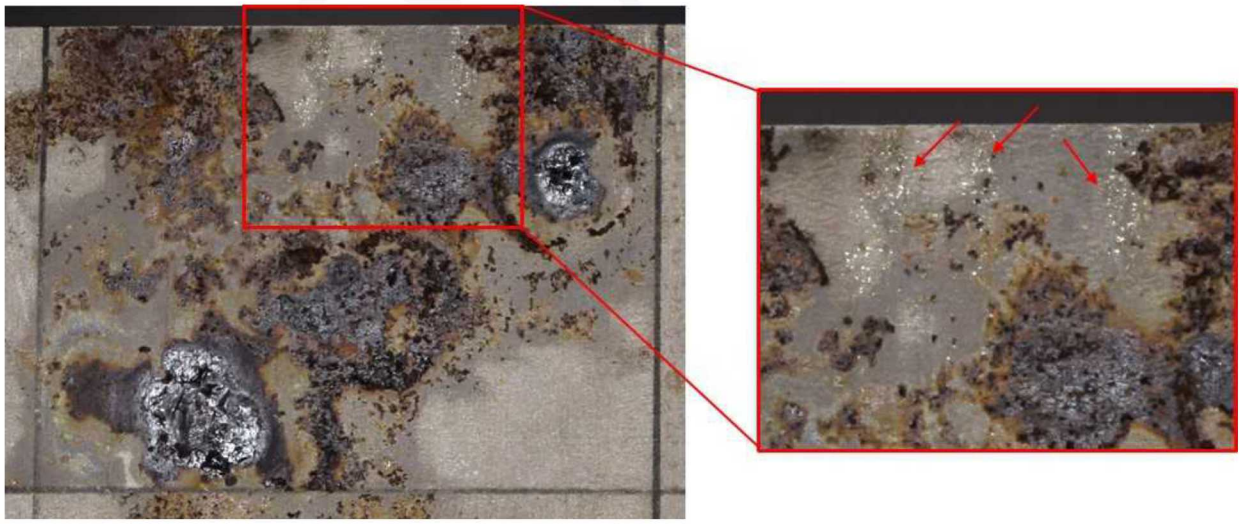

Figure 20. White residue surrounding corroded areas in Quadrant 1 of the 4-point bend specimen.

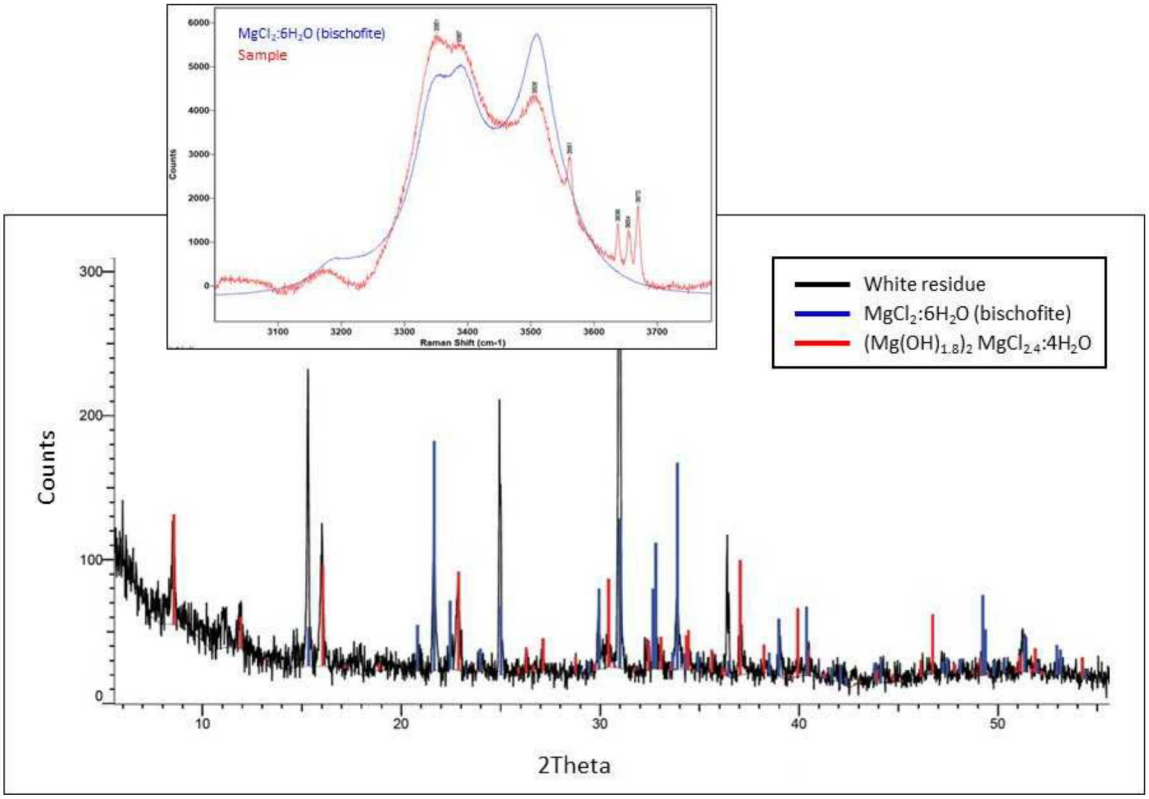

Figure 21. X-ray diffraction indicates residue contains a magnesium hydroxychloride, approx. $Mg(OH)_2)_2MgCl_2{:}4H_2O$. Raman-spectrum (inset), shows sharp peaks between 3500 and 3700 wave-numbers, confirming the presence of a hydroxyl phase.

2.1.3 Implications of Brine Stability Studies

The brine stability tests and the analysis of the salt residue from the corroding metal surfaces demonstrate that magnesium chloride brines are not stable at elevate temperatures. In contrast to FY17 tests, the brine was not evaluated at conditions relevant to a SNF storage canister surface---while canister surfaces easily exceed 80°C, RH conditions on a canister surface at that temperature would be far below the deliquescence point of magnesium chloride. Instead, we evaluated magnesium chloride brine stability under conditions that have been used, and are being used, for accelerated corrosion testing by SNL and others. The goal of these experiments was to assist in interpretation of data produced by accelerated (elevated temperature) testing protocols, to aid in design of such experiments, and to provide a basis for extrapolation of experimental results to *in situ* conditions on the canister surface. In FY 19, we will work to develop a fundamental understanding of the magnesium chloride-magnesium hydroxychloride-magnesium carbonate system by development of a thermodynamic model for the system. This work will also provide information on the deliquescence properties of these materials. Further experimental work will characterize reaction products, both on inert substrates and on actively corroding steel surfaces.

The processes evaluated here are enhanced by elevated temperatures, which promote acid gas evolution from the brine. At ambient temperatures, particle-gas exchange reactions with acid gases in the atmosphere, including sulfuric acid (or SO_2) and nitric acid (or NO_X) are widely recognized to result in chloride loss form sea-salt aerosols. IN FY 19, we will also begin evaluating these reactions through thermodynamic modeling.

2.2 Analysis of Samples Collected from In-Service Storage Canisters at the Maine Yankee ISFSI

In July, 2018, the Management and Operations contractor at the Maine Yankee Independent Spent Fuel Storage Installation, located near Wiscasset, Maine performed an inspection on a SNF dry storage canister within its overpack. As part of that inspection, the overpack lid and shield plug were removed, and samples of dust were taken by hand from the upper surface of the canister. These samples were sent to SNL for analysis.

This sampling complements one that was carried out in July of 2016, in which samples were collected from surfaces within a different storage system. Because the primary goal of that field test was to evaluate the use of robots in surveying the surface of the canister within the overpack, collection of dust samples was carried out in a qualitative fashion, using paper filters and sponges as the sampling media. The sampling focused mostly on determining the composition of soluble salts present in the dust. It was anticipated that a wet substrate would more effectively extract soluble salts from the surface, so both the sponges and the filter paper were wetted with demineralized water prior to being applied to the surface of the metal. Sampling was accomplished by simply pressing the damp substrate against the metal surface for two minutes, and then removing it. It is unlikely that the sampling method quantitatively collected dust or salts from the metal surface. Samples were collected from the top of the shield plug, from a shelf near the bottom of the overpack, and one sample was collected from the side of the canister.

In the current sampling episode, the samples provided to SNL were collected from the top of the canister. They included wet samples collected to measure the soluble salts present, and dry samples used to evaluate dust and salt mineralogy, morphology, and distribution. The wet samples were collected with a moist sponge; the dry samples were collected with a Scotchbrite™ pad, brushed over the surface.

2.2.1 Samples

Two types of samples were collected from the in-service dry storage canister at the Maine Yankee Nuclear Facility. The first type consisted of pieces of Scotch-Brite™ abrasive pad, that were swept across the metal surface by hand, and then placed in a polypropylene compartmentalized box with double-stick tape in each compartment, and double-bagged in Ziploc® bags with a desiccator cartridge for shipment to SNL. The second type of sample consisted of damp polyurethane sponge material made by Truclean®; in order to make the sampling quantitative, each sample was used to remove the salts and dust from a 6” × 6” cm area delineated using a plastic template, taking care to remove all dust. Each sponge was then then inserted into a 50 ml polypropylene tube. Both the Scotch-Brite™ and sponge samples were placed in a cooler with Blue Ice® and shipped via overnight express to SNL. Upon arrival, the pads were immediately placed in a desiccator, and the sponges in a refrigerator until the salts were extracted on the following day.

Both of the sampling materials were provided to Maine Yankee by SNL, the Sctoch-Brite™ as a pad 6” × 9” in size, and the sponge material as a rectangular sponge 2” × 4” × 8” in dimension. Both had been repeatedly rinsed with deionized water prior to sending in an effort to remove any salts present in or on the material itself. For use, the Scotch-Brite™ pad was cut into several 2” × 2” pieces. The pieces were not labeled, and upon delivery, were treated as a single sample, with randomly chosen samples examined by SEM. The sponge had been cut into slices either 2” × 4” × 1” or 2” × 4” × 1.25” in size. SNL received six unnumbered samples; a number was assigned to each, and each was handled as a separate sample. No blanks were provided, so to determine the amount of salts that might leach out of the sponge material itself, an additional sponge was rinsed with deionized water in a manner similar to the first, and cut into similar-sized pieces. Five of these were used as blanks. As discussed later, the very large size of the individual sample sponges (much larger than had been previously used in 2016) resulted in significant blank values. To measure the soluble salts, all samples and blanks were placed in 50-70 mL

deionized water and repeatedly compressed to homogenize the water inside and outside of the sponge. The water was then extracted and analyzed to determine the total soluble salt content.

2.2.2 Methods

The following methods and equipment were used to characterize the samples from Maine Yankee:

- *SEM imaging and EDS element mapping*. SEM/EDS analysis of the dry dust samples provided textural and mineralogical information on the mineral and salt phases present, and allowed visual identification of organic matter (floral/faunal fragments).
- *Chemical analyses of the soluble salts in the dust.* As described in Section 2.2.1, soluble salts were leached from the sponges and analyzed to determine their concentration and composition.

SEM Imaging and EDS Analysis

SEM/EDS analysis of the samples provides textural and mineralogical information on the dust, and allows visual identification of organic matter (floral/faunal fragments). Sample fractions retained for SEM analysis were coated with gold/palladium to reduce sample charging during analysis. Imaging and element mapping was done with a Tescan Vega3 SEM, equipped with an EDAX Element® EDS detector. An accelerating voltage of 15 keV was used, and working distances of 9 to 12 mm, with varying degrees of magnification. Images were obtained using both secondary and backscattered electron imaging, and a beam current of 100-200 pA. A somewhat higher beam current (1 nA) was used to produce a high count rate during EDS analysis and to facilitate rapid element mapping.

Chemical Analysis

The sponge samples were leached in a known volume of deionized water to extract the soluble salts. Sponge blanks prepared at SNL were similarly leached to determine background salt compositions and concentrations. The solutions were filtered through 0.45 µm syringe filters and 5 mL aliquots were immediately transferred to sample vials for analysis by IC. All sponge samples and blanks were then dried and weighed to determine sample mass, so that blanks could be appropriately subtracted, as the cut sponge pieces used in sample collection varied in size and weight. However, although blank values were significant, there was no systematic variation with sponge size, so the average of the blank values was subtracted from each sample instead.

Soluble salt compositions were determined by ion IC analysis. Anionic analytes were F^-, Cl^-, Br^-, NO_2^-, NO_3^-, SO_4^{-2}, and PO_4^{-3}; however, Br^- and NO_2^- were never detected, and are not included here. Cationic analytes were Li^+, Na^+, NH_4^+, K^+, Mg^{2+}, and Ca^{2+}. For detailed analytical procedures, see Bryan and Enos (2016). All analyses were carried out using standards made by dilution of Dionex standards. All standards and electrolytes were purchased specifically for this analysis, and were within their expiration date.

2.2.3 Results

2.2.3.1 SEM/EDS Analysis of Insoluble Mineral Residue

SEM/EDS analysis of the dry dust samples was carried out to determine the composition and morphology of the insoluble phases and of the soluble salts. Analyzed samples include small pieces cut from three of the Scotch-Brite™ pads. Very fine dust particles adhered to the fibers of the Scotch-Brite™ pads, but copious amounts of coarser particles fell though and accumulated in the compartmentalized polypropylene storage box; for this reason, a SEM mount was also made of loose particles that had dislodged from one of the pads and accumulated in the plastic compartment. Results are summarized here, with typical images from the samples.

Typical SEM images of the coarse particulates that fell though the Scotch-Brite™ pad are shown in Figure 22. Close-ups of individual grains are shown in Figure 23. Much of the material consists of fibrous plant matter, frequently displaying a starlike morphology; these are stellate trichomes, structures common on oak leaves. Also present in abundance are pollen grains, appearing as spongy ovoids. Rare diatoms and phosphatic animal matter were also observed. Detrital mineral grains were abundant, consisting dominantly of large platy flakes of mica, which are identified as biotite on the basis of composition, and detrital grains of potassium aluminosilicate (potassium feldspar), calcium and sodium aluminosilicate (plagioclases), and quartz. Some more mafic (Fe-Mg rich) silicates were also present, and rare grains of zircon, iron oxide, and titanium oxide. Anthropogenic particles included rare steel shavings and spheriodal particles of iron-chrome oxide produced by welding. Detrital calcium carbonate grains were relatively common; and rare Ca-Mg-carbonate (dolomite). In the previous Maine Yankee inspection (Bryan and Enos, 2016), particles derived from efflorescence formed by seepage from the concrete overpack were abundant, in the form of well-crystallized plates of calcium carbonate, calcium silicate, and calcium aluminum silicate were abundant. Concrete efflorescence was also observed in the dust collected during this sampling episode (Figure 24), consisting of well crystallized plates of calcite, in some cases with associated gypsum.

Measured soluble ions are described in the next section, but include relatively high levels of calcium, sodium, potassium, magnesium, nitrate, chloride, and sulfate; however, the deficiency of measured anions indicates that carbonate is a major component of the soluble anions as well. Calcium carbonate is the most abundant carbonate phase, but minor dolomite (calcium magnesium carbonate) was also observed. Gypsum was the only sulfate. No salt phases containing nitrate, potassium, or magnesium were found, but this may have been because of the obscuring effects of the minerals (rich in potassium and magnesium) and the plant matter (rich in nitrate). Chloride was observed as NaCl, which frequently occurs associated with plant matter (Figure 25 and Figure 26). Rarely, KCl was also present. Nearly all the plant matter present had associated chloride X-ray peaks; in some cases, chloride was visible as a separate phase adhering to the material, but frequently, it was disseminated finely on the surface of the plant matter, making imaging of individual grains difficult.

Material on the Scotch-Brite™ pads was also analyzed. The pads are made of nylon fibers and alumina abrasive embedded in epoxy. The pads are highly porous, and the coarser detrital mineral grains and almost all the plant material, including most of the pollen, simply fell through the pad to the bottom of the compartment containing the pad in the storage box. However, particles less than 20μm adhered to the nylon fibers in the pads well, allowing examination of the finest particles present in the dust. These particles were mostly fine detrital mineral grains and clusters of clay minerals. Chloride was present as NaCl, dominantly associated with very fine-grained clay mineral aggregates (Figure 27 and Figure 28).

While the dominant components of sea-salts are present in the soluble salts, sea-salt aerosols as seen previously at Diablo Canyon (Bryan and Enos, 2014) were not observed. Typically, sea-salt aerosols are clusters of salts—sodium chloride and magnesium sulfate (the dominant species present in sea water) with minor calcium and potassium species—in the size range of 5-15 μm, whereas here, the observed chloride salts were much finer grained, and commonly adhering to large but low-density particles of organic matter or fibers, or to mineral aggregates. This is important to consider both when estimating the deliquescence properties and corrosiveness of the salts, and when estimating salt transport and deposition within the overpack, important considerations for predicting potential SCC of the canisters.

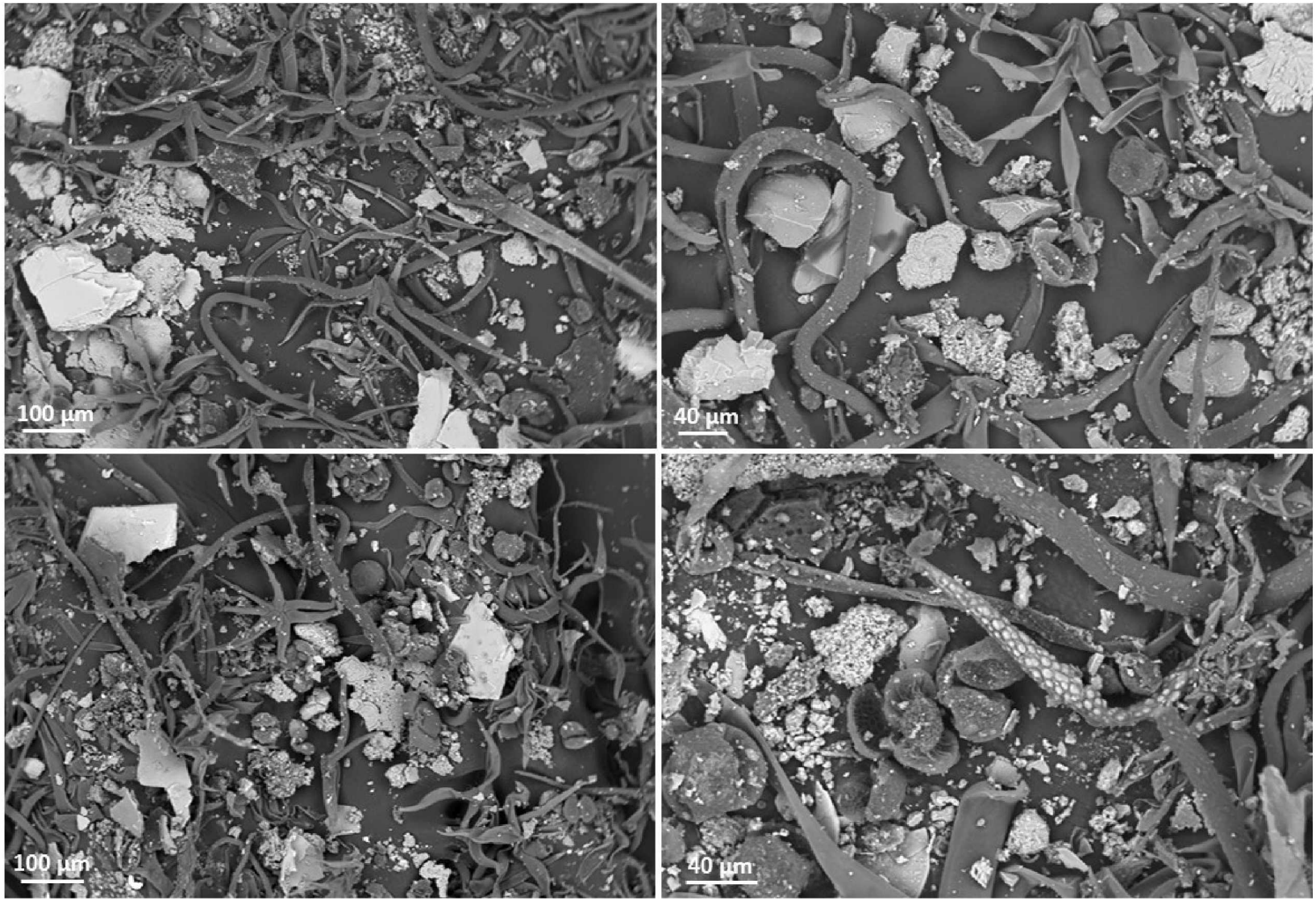

Figure 22. SEM BSE images of coarse particulates from the surface of the Maine Yankee storage canister.

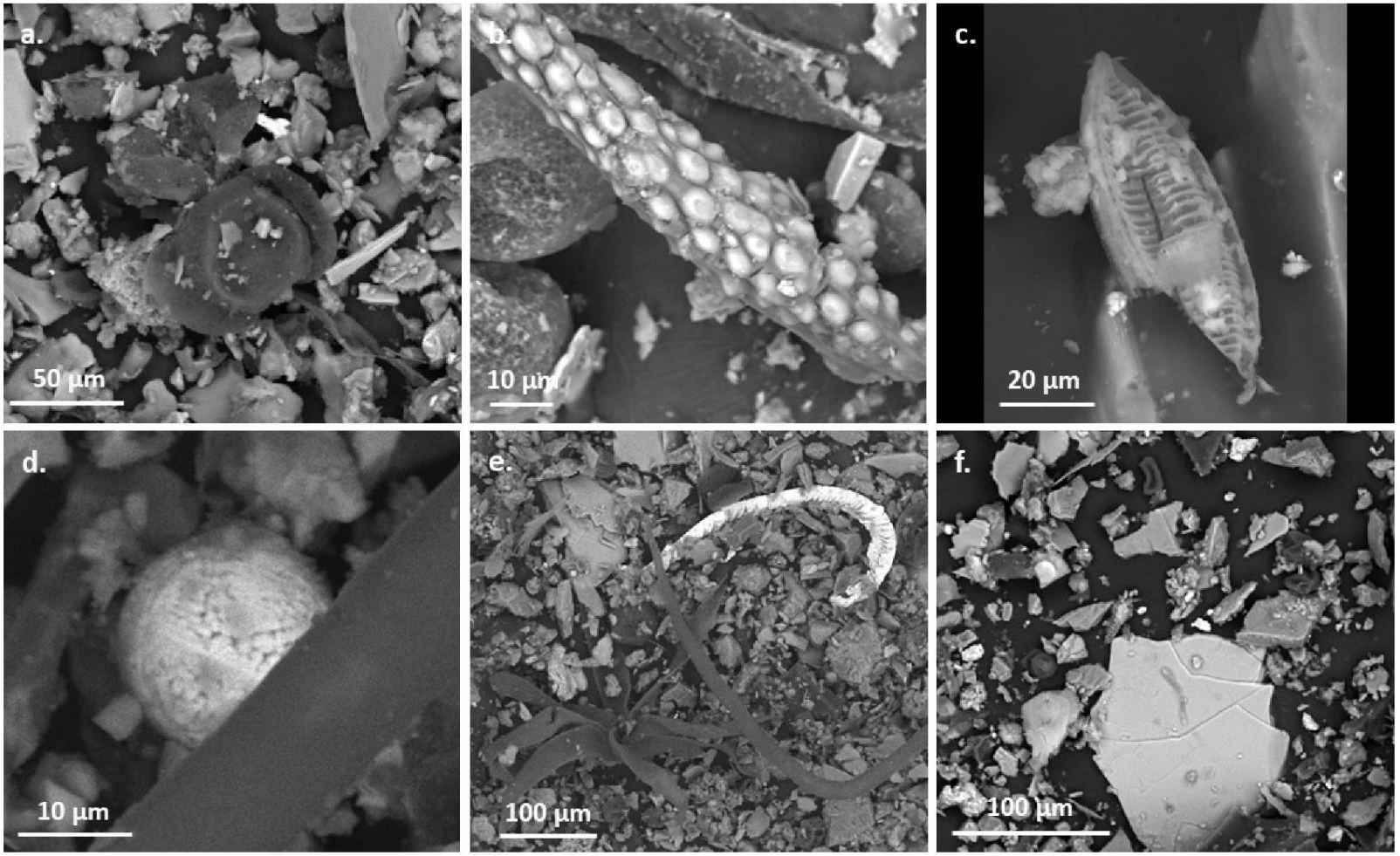

Figure 23. High magnification SEM BSE images of coarse particulates from the surface of the Maine Yankee storage canister. (a) pollen grains; (b) phosphatic arthropod(?) fragment; (c) diatom; (d) iron-chrome oxide sphere (oxidized welding spatter); (e) steel shaving; (f) mineral grains, including coarse plate of biotite.

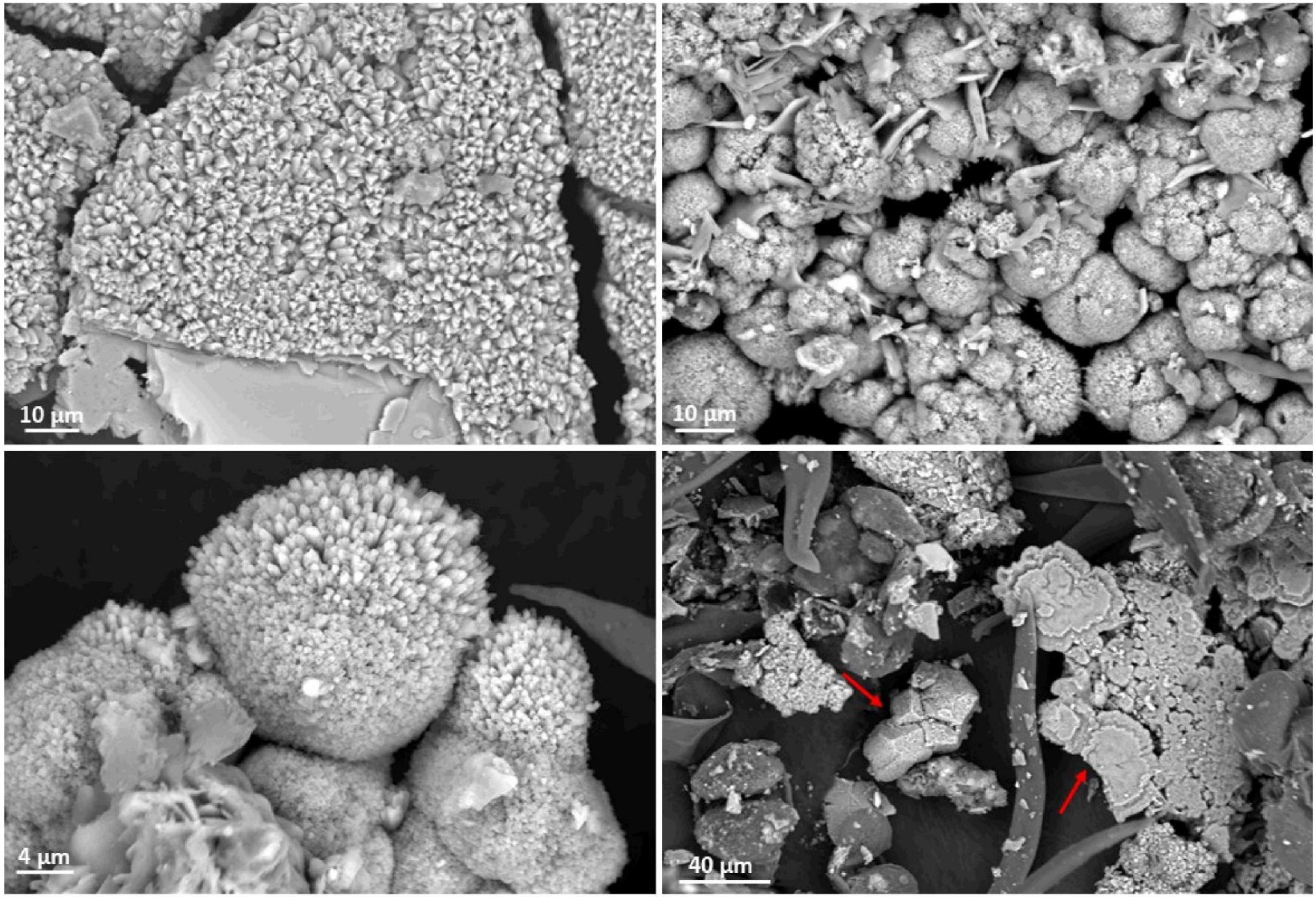

Figure 24. SEM BSE images of concrete efflorescence in the dust. (a) flat plate of calcite crystals; (b) botryoidal calcite with gypsum blades; (c) botryoidal calcite with bladed gypsum and calcium aluminum silicate; (d) well formed calcite crystal, with a concentrically grown plate of calcite.

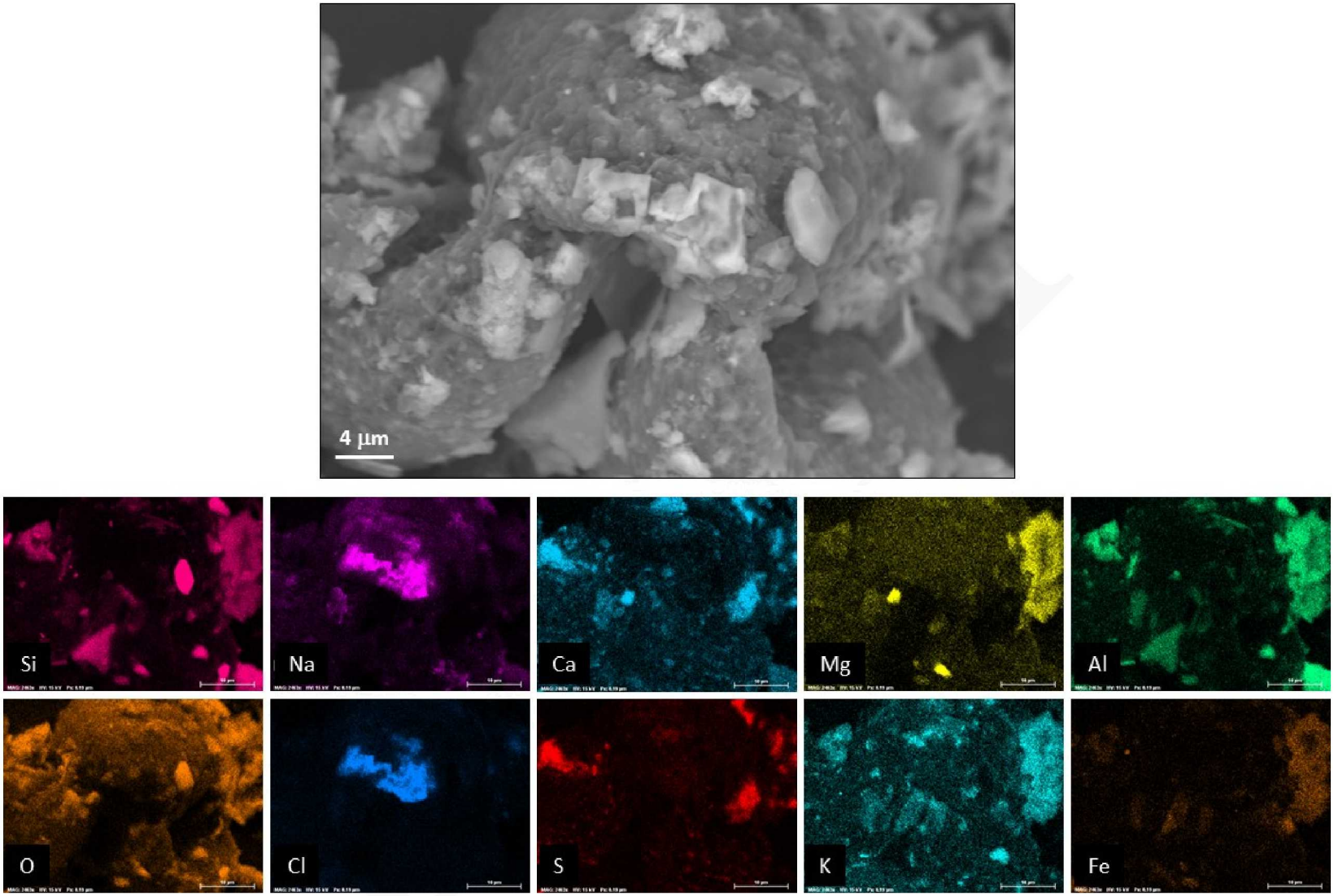

Figure 25. SEM BSE image and EDS element maps of NaCl adhering to the porous surface of a pollen grain.

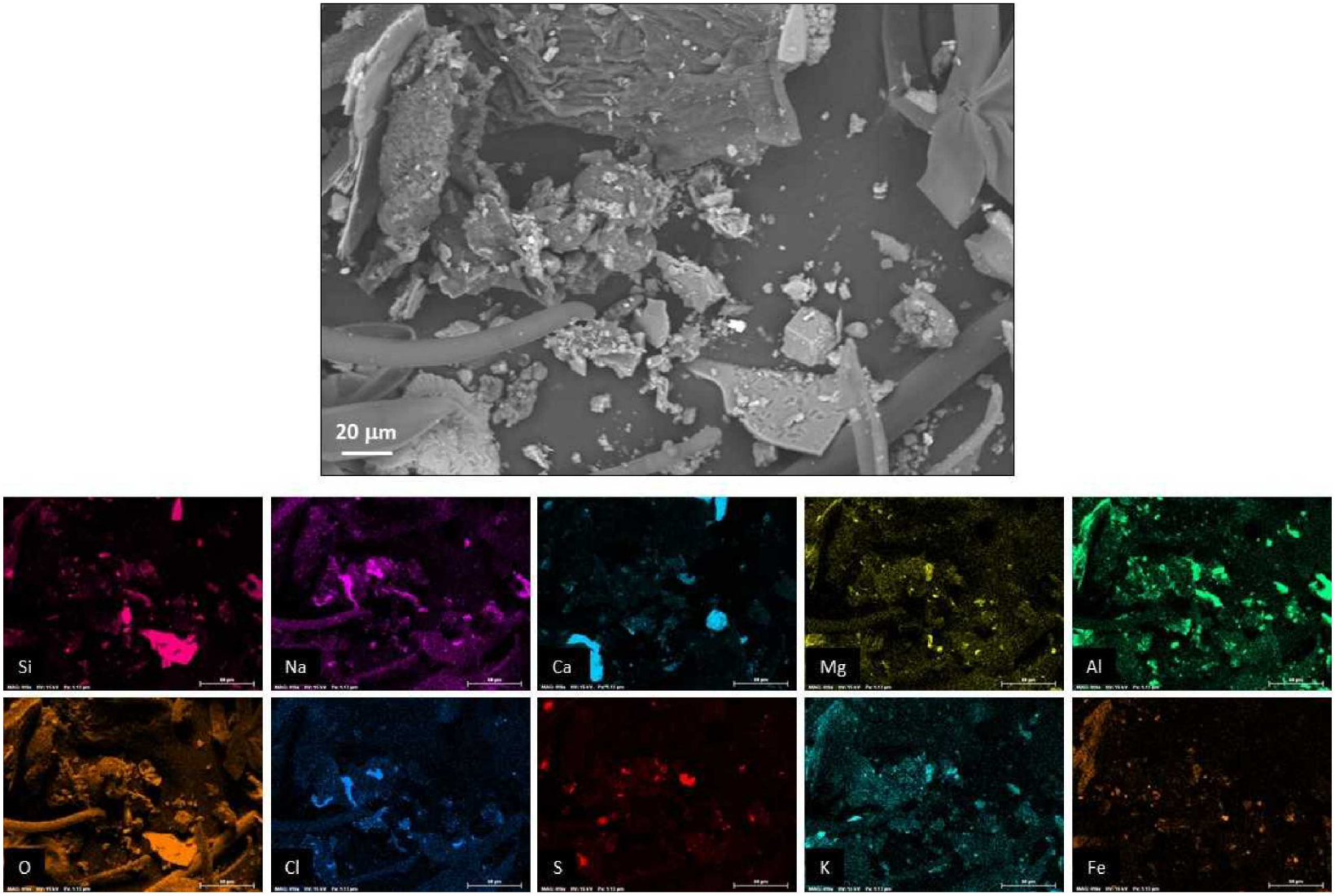

Figure 26. SEM BSE image and EDS element maps of NaCl adhering to the porous surface of a pollen grain, and to clusters of clay minerals.

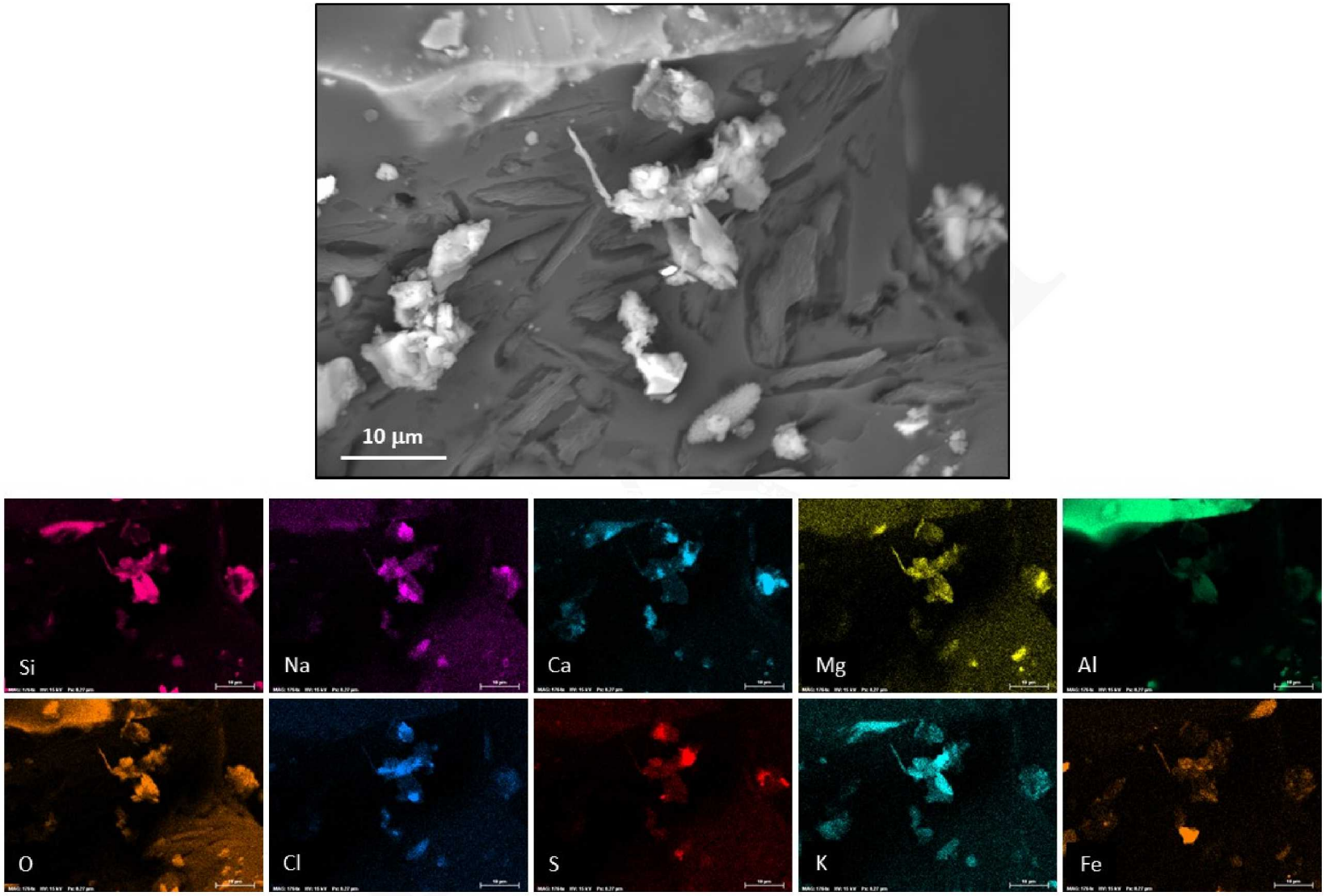

Figure 27. SEM BSE image and EDS element maps of NaCl associated with fine-grained mineral clusters.

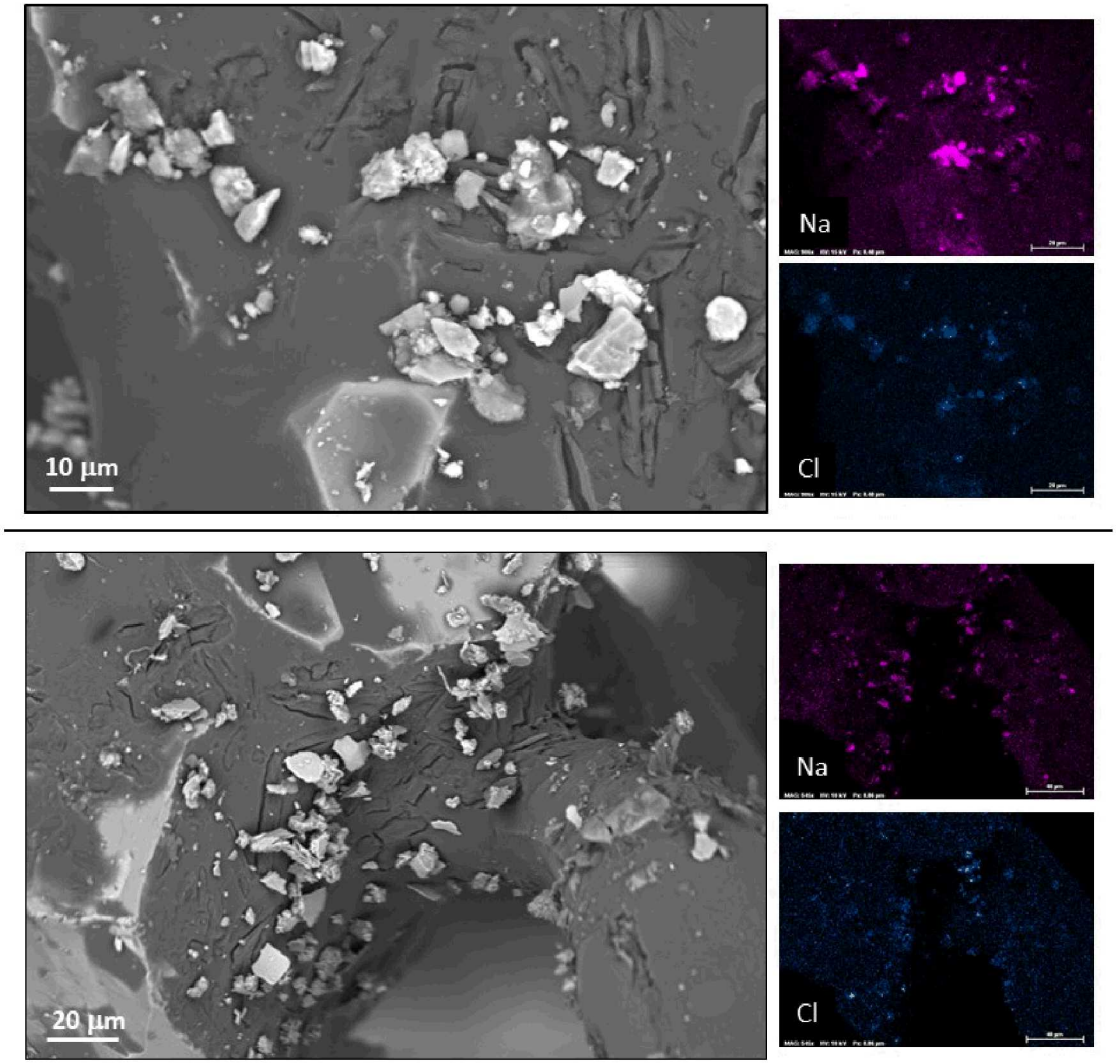

Figure 28. SEM BSE images and EDS element maps of NaCl associated with fine-grained mineral clusters.

2.2.3.2 Chemical Analysis of Soluble Salts

As noted previously, six unnumbered samples were provided to Sandia for chemical analysis. These were numbered 1-6, and analyzed separately. In addition, 5 sponge blanks were created at SNL, to evaluate and account for soluble salts that might leach from the sponge material.

The soluble ion concentrations in the sponge blanks, in µg/sample, are shown in Table 1, and ion concentrations for the samples from the top of the overpack are shown in Table 2. Values shown in italicized gray type had clearly defined IC peaks, but fell between the lowest standard and the blank, and are semi-quantitative. Measurement uncertainties are generally 5% or less, but may be as high as 20% for low values, near the quantitation limit. The blank values were relatively high, due to the large size of the sponge pieces used, and showed considerable variability. Relative to four of the samples, the values for the sponge blanks were insignificant. However, for two samples (MY-3 and MY-4), the measured concentrations for several elements were only slightly higher than were observed in the blanks. This can be seen in Table 3, where the average sponge blank values have been subtracted from the sample values for each element.

The salt concentrations in micro-equivalents (µEq) per sample are provided in Table 4. The number of µEq is equal to the number of µmoles multiplied by the charge of the ionic species; relative to µg, this unit eliminates the effect of different masses for the ionic species, providing a clearer understanding of the relative importance of each species with respect to the total ion load.

The charge balance error is calculated from the total cationic and anionic µEq present using:

$$Charge\ balance\ error, \% = \frac{(Sum\ of\ cations - Sum\ of\ anions)}{(Sum\ of\ cations + Sum\ of\ anions)} \times 100$$

As has been previously observed for soluble salt analyses at Calvert Cliffs, Hope Creek, Diablo Canyon, and the previous analyses from Maine Yankee (Enos et al., 2013; Bryan and Enos, 2014; EPRI, 2014; Bryan and Enos, 2015a; Bryan and Enos, 2016), the charge balance is poor; measured anion µEq are much less than cation µEq. This has previously been attributed to carbonate species, both because carbonate cannot be measured in the IC analyses, and because carbonates have been commonly observed in SEM analyses of the dusts (Enos et al., 2013; Bryan and Enos, 2014; EPRI, 2014; Bryan and Enos, 2015a). Calcium carbonate in the form of cement efflorescence was observed in the dust collected in 2016 (Bryan and Enos, 2016), as well as in this sampling episode. Hence, carbonate is also likely to be responsible for the majority of the charge imbalance in the Maine Yankee samples. However, organic material constitutes a large fraction of the dust, and soluble salts of organic compounds may also be contributing to the ion load, and to the charge balance error since such anionic compounds were not measured.

Scatterplots of each soluble species concentration, plotted against Na, are shown in Figure 29. Except for Ca, which is more scattered, concentrations vary directly with that of Na, and form a linear trend intersecting near zero. This strongly suggests that the soluble component in all samples has a constant composition presumably representing soluble aerosol compositions at the site, and that only the amount of deposited material varies. The greater variability in calcium may reflect the local source for that species (concrete efflorescence) within the overpack.

Compositionally, the soluble components are similar in all samples, with Ca dominating the cations. Na is the second most abundant cation. In terms of molar concentrations, K and Mg are present in similar concentrations, both far too high to be representative of sea water, if we assume that the source of the sodium is sea-water. Among the measured anions, sulfate is the most dominant species. Nitrate and chloride are next, present in subequal amounts in terms of moles. Fluoride was present in measurable

amounts; the source for this is unknown. As noted earlier, large anion deficiencies in the analyses indicate that carbonates are probably the most common component in soluble salts the dusts, although given the abundance of organic material, anionic organic salts cannot be ruled out.

In single-chloride salt systems, chloride surface load has been related to likelihood of SCC. The presence of other anions is frequently considered to be mitigating, but the chloride surface load is still taken to be an indicator of SCC risk. Measured chloride surface densities for the Maine Yankee canister top samples are provided in Table 5. The maximum chloride surface load is quite low, about 75 mg/m^2. This is a very low load, but SCC has been observed at lower values.

The salt compositions suggest that the soluble salts are a combination of both sea-salts (rich in Na, Cl, and Mg), and salts derived from continental sources, rich in NH_4, K, Ca, NO_3, and SO_4, although NH_4 was not observed here. Although K and Mg are present in sea-salts, here they are far too enriched relative to Na to be derived from sea-salts. There are several possible explanations for the lack of ammonium. The absence of ammonium is consistent with experimental evidence that it does not persist in the presence of nitrate or chloride, because it is lost from the surface via a coupled degassing reaction (Bryan and Enos, 2015b; Bryan and Enos, 2015a; Enos and Bryan, 2016b). Moreover, if unreacted cement phases were present in the dust and in contact with the deliquesced salts, then the resulting high pH would have promoted conversion of NH_4^+ to NH_3, further driving degassing. Finally, ammonium may have been lost by degassing from the moist sampling media during sample storage and transportation.

It is reasonable to assume that most of the chloride was deposited as sea-salts, and indeed, chloride and sodium are present in very similar amounts in most samples. When found as a discrete salt phase, chloride was present as NaCl. However, most of the chloride appeared to be present as disseminated species associated with plant matter and fine-grained mineral (clay) particles. It was not possible to identify the form of the chloride on that material. The plant matter and clay particles may be marine in origin, or may simply have been contacted by marine aerosols, either before or after becoming aerosolized themselves.

Table 1. Soluble Ion Concentrations in Sponge Blanks, µg/sample.

Sample #	Na^+	NH_4^+	K^+	Mg^{2+}	Ca^{2+}	F^-	Cl^-	NO_3^-	PO_4^{3-}	SO_4^{2-}
SB-1	16.4	*1.7*	34.0	1.3	47.4	*0.2*	56.6	67.7	*2.5*	7.5
SB-2	7.9	*0.9*	17.2	*0.5*	36.5	*0.3*	43.8	29.6	*2.0*	2.4
SB-3	8.2	*0.9*	13.9	*0.4*	27.2	*0.3*	46.5	14.3	n.d.	1.8
SB-4	7.6	*1.6*	15.4	*0.4*	34.6	0.4	54.3	24.9	n.d.	2.4
SB-5	5.3	*1.3*	9.5	*0.1*	33.5	*0.4*	48.4	7.9	n.d.	*1.2*
Averages	9.1	*1.3*	18.0	*0.5*	35.8	*0.3*	49.9	28.9	2.2	3.1

Note: Values shown in italicized gray type had clearly defined IC peaks, but fell between the lowest standard and the blank and are semi-quantitative.

Table 2. Soluble Ion Concentrations in Maine Yankee Dust Samples, µg/sample.

Sample #	Na^+	NH_4^+	K^+	Mg^{2+}	Ca^{2+}	F^-	Cl^-	NO_3^-	PO_4^{3-}	SO_4^{2-}
MY-1	182	*0.7*	110	27.3	735	14.8	180	289	9.8	203
MY-2	177	3.4	111	21.0	844	30.8	152	325	7.3	190
MY-3	37.6	*0.8*	21.8	8.8	198	12.7	70.8	36.5	n.d.	30.7
MY-4	51.0	*1.0*	35.5	n.d.	143	11.4	70.2	91.0	n.d.	33.9
MY-5	126	*0.5*	74.1	22.9	456	29.6	164	136	n.d.	196
MY-6	364	*0.9*	246	49.1	782	33.7	318	514	15.3	453

Note: Values shown in italicized gray type had clearly-defined IC peaks, but fell between the lowest standard and the blank, and are semi-quantitative.

Table 3. Blank-Subtracted Soluble Ion Concentrations in Maine Yankee Dust Samples, µg/sample.

Sample #	Na^+	NH_4^+	K^+	Mg^{2+}	Ca^{2+}	F^-	Cl^-	NO_3^-	PO_4^{3-}	SO_4^{2-}
MY-1	173	n.d.	91.6	26.7	699	14.4	130	260	7.5	199
MY-2	168	2.1	92.7	20.4	808	30.5	102	296	5.0	187
MY-3	28.5	n.d.	3.8	8.2	162	12.4	20.9	7.6	n.d.	27.6
MY-4	42.0	n.d.	17.5	n.d.	107	11.0	20.3	62.1	n.d.	30.8
MY-5	117	n.d.	56.2	22.3	421	29.3	114	108	n.d.	193
MY-6	355	n.d.	228	48.5	746	33.4	268	485	13.1	450

Note: Values shown in italicized gray type had clearly-defined IC peaks, but fell between the lowest standard and the blank, and are semi-quantitative.

Table 4. Soluble Ion Concentrations in Maine Yankee Dust Samples, µEq/sample.

Sample #	Na^+	NH_4^+	K^+	Mg^{2+}	Ca^{2+}	F^-	Cl^-	NO_3^-	PO_4^{3-}	SO_4^{2-}	Cations	Anions	CBE%
MY-1	7.5	n.d.	2.3	4.4	69.8	0.8	3.7	4.2	0.9	8.3	84.0	17.8	65%
MY-2	7.3	0.1	2.4	3.4	80.7	1.6	2.9	4.8	0.7	7.8	93.7	17.7	68%
MY-3	1.2	n.d.	0.1	1.4	16.2	0.7	0.6	0.1	n.d.	1.2	18.9	2.5	76%
MY-4	1.8	n.d.	0.4	n.d.	10.7	0.6	0.6	1.0	n.d.	1.3	12.9	3.4	58%
MY-5	5.1	n.d.	1.4	3.7	42.0	1.5	3.2	1.7	n.d.	8.0	52.2	14.5	56%
MY-6	15.4	n.d.	5.8	8.0	74.5	1.8	7.6	7.8	1.5	18.8	103.8	37.3	47%

Notes: Values shown in italicized gray type had clearly defined IC peaks, but fell between the lowest standard and the blank, and are semi-quantitative.
CBE = charge balance error, %.

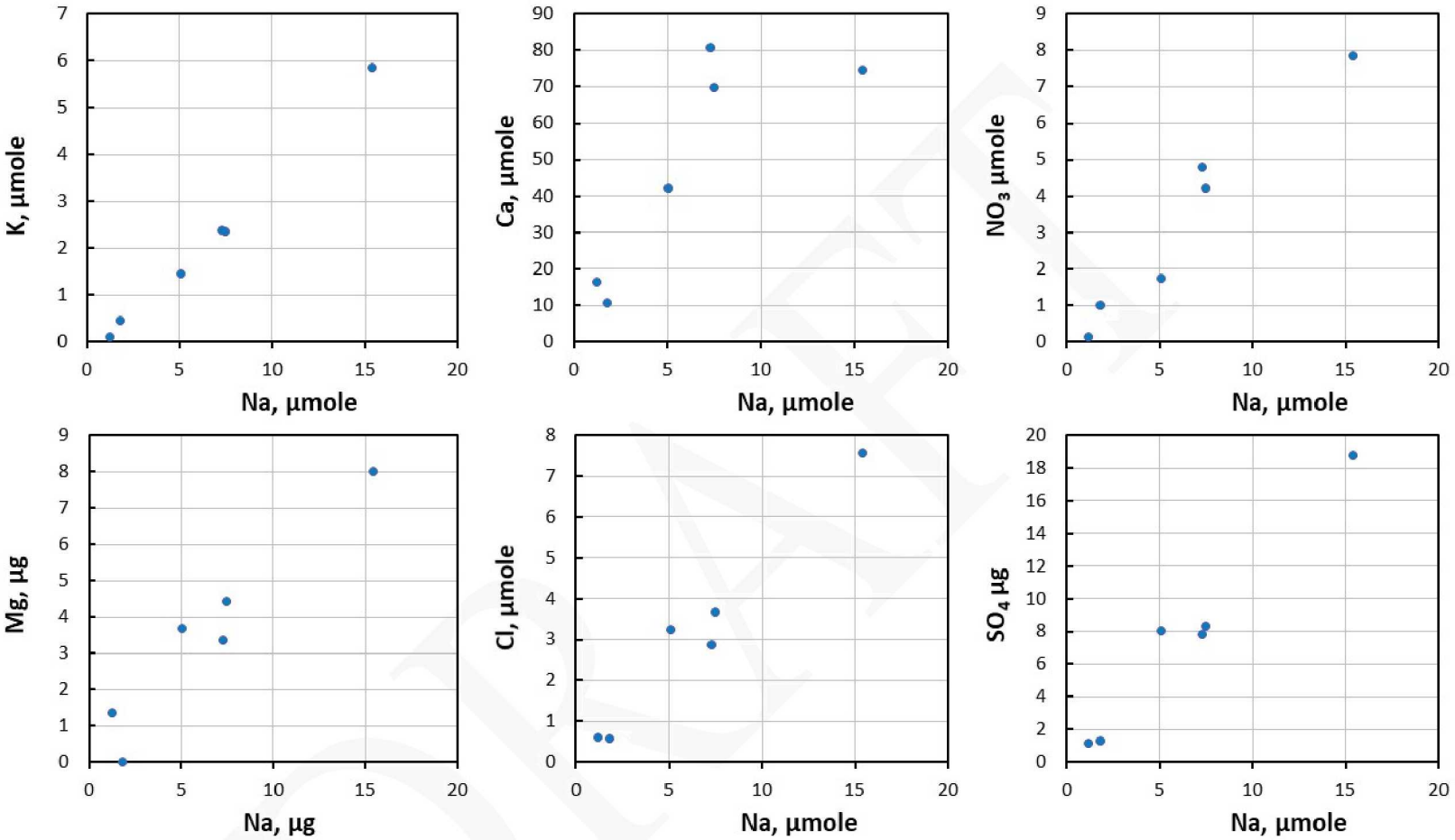

Figure 29. Scatterplots of soluble species, each species plotted against Na concentration. The plots show a strong linear trend, intersecting the y-axis near zero.

Table 5. Measured Chloride Surface Densities, mg/m^2.

Sample #	Cl⍰, mg/m^2
MY-1	36.0
MY-2	28.3
MY-3	5.8
MY-4	5.6
MY-5	31.8
MY-6	74.4

2.2.4 Summary of Maine Yankee Dust Samples

Analysis of the Maine Yankee dust samples provided important information about the chemical environment on the surface of the canisters at the site. Soluble salts are present in significant amounts in the dust, and are dominated by sulfates and nitrates. However, chloride is present in significant amounts, occurring as sodium chloride and commonly associated with coarse plant fibers and pollen in the dust, and with fine aggregates of silicate minerals, likely clays. Sea-salt aerosols were not observed. The association of chloride salts with other particulates must be considered when evaluating salt transport and deposition phenomena both externally and within the overpack, as the aerodynamic properties of the materials will vary from those of standard sea-salt aerosols or deliquesced droplets.

The composition of the soluble component appears to be relatively consistent in the six samples collected, with only the amount present varying. The composition and relative species concentrations (ion ratios) indicate that sea-salts alone cannot account for the observed salts, and that a large component of continental-salt aerosols is present. Measured chloride surface loads are low, with the highest values being less than 0.1 g/m^2. Salt load is an important risk factor for SCC, and low values such as these are generally considered to be beneficial. The potential role of other soluble components in mitigating or increasing SCC risk is not known.

3 RELATIONSHIP BETWEEN CORROSION DAMAGE AND SURFACE ENVIRONMENT

Development of probabilistic and deterministic SCC models to assess risk and guide inspection of SNF interim storage canisters requires (1) an improved understanding of how surface environment relates to damage evolution in canister-relevant conditions, and (2) datasets that relate extent of damage to measurable surface environment parameters (e.g. RH, T, salt load). Information in both areas is lacking in the literature with respect to canister-relevant conditions. This thrust aims to experimentally define the relationship between environment and localized corrosion and SCC damage kinetics and distributions in simulated near-marine environments.

3.1 Pitting Kinetics and Damage Distributions

Work in FY18 has continued with a series of experiments to quantify damage that evolves on austenitic stainless steels exposed to ISFSI-relevant fixed humidity and temperature conditions. These experiments are being utilized to develop datasets on pit frequency and size distributions as a function of time and environment. This data will be utilized to inform and benchmark statistical and deterministic SCC models under development at SNL, OSU and CSM.

In FY17 Q2 – 304L coupons loaded with ASTM D1141 artificial sea salt were placed in environmental chambers for exposure at two RH and temperature conditions for up to two years. Sets of coupons are being removed periodically to measure corrosion damage using optical profilometry. This work is being carried out with Prof. Jenifer Locke and The Ohio State University. The environmental conditions relevant to expected canister conditions are shown in Table 6; at absolute humidities that occur naturally, the greyed-out combinations of temperature and RH are not predicted as achievable on the canister surface. The remaining conditions represent the range of environments at which deliquesced brine could occur on the canister surface. Highlighted in green are the two conditions currently under test. These represent two humidity conditions where we would expect potentially severe pitting. At 40% RH, conditions are just above the deliquescence RH for magnesium chloride at this temperature (~36% RH), resulting in a highly concentrated but small volume of magnesium-chloride rich brine. At 75% RH, the seawater brine is comprised of a much larger volume of near-saturated NaCl (~6 M). Artificial sea salt loadings of 10 and 300 µg/cm^2 were chosen for this test, representing a values within the lower and upper bounds reportedly measured on canisters or surrogate surfaces in marine conditions (EPRI, 2015).

Table 6. Expected Corrosive Environmental Conditions on Canister Surfaces

%RH	Temperature (°C)				
75	35				
70	35				
65	35				
60	35				
55	35	40			
50	35	40			
45	35	40	45		
40	35	40	45		
35	35	40	45	50	
30	35	40	45	50	

Rectangular coupons measuring 1" x 2" with either one of two surface finishes are being examined, a mirror finish (R_a = 0.05 µm) and a 120 grit "mill" rough finish (R_a = 2.8 µm). The latter was chosen as the expected upper bound of roughness on the as-built canister surfaces. The mirror finish was chosen as it provides a uniform background ideal for pit analysis using optical profilometry and could be used to analyze the surface chemistry that develops from corrosion. Thus, these two surface finishes represent two extreme bounds of roughness on the expected canisters. Surface finish is expected to have considerable impact on pitting kinetics and size distributions (Burstein and Pistorius, 1995; Moayed et al., 2003). Rougher surfaces are generally more prone to pit initiation, which has been attributed to occluded regions in the ground surface and, possibly, localized residual stress/strain that can act as pit initiators.

The experimental approach emphasizes a novel, high-throughput sample preparation and analysis methodology to address the parameter space under exploration and need for statistically relevant datasets. An inkjet printing technique is utilized for rapid and rigorously controlled deposition of ASTM D1141, artificial seawater (ASTM International, 2008) particles on the sample surfaces (Schindelholz and Kelly, 2010b). Using this unique capability, we can prepare hundreds of samples per day. The salt loading pattern on the coupons for two different loading densities is shown in Figure 30. Corrosion damage morphology (e.g. pitting) is analyzed using a white light profilometer at OSU to create 3D profiles of the exposed coupons. The profiles are analyzed using a commercial software package capable of automatic detection and measuring of individual pit features. Combined, these capabilities enable us to develop statistically relevant datasets on pit frequency, size and shape distributions over time.

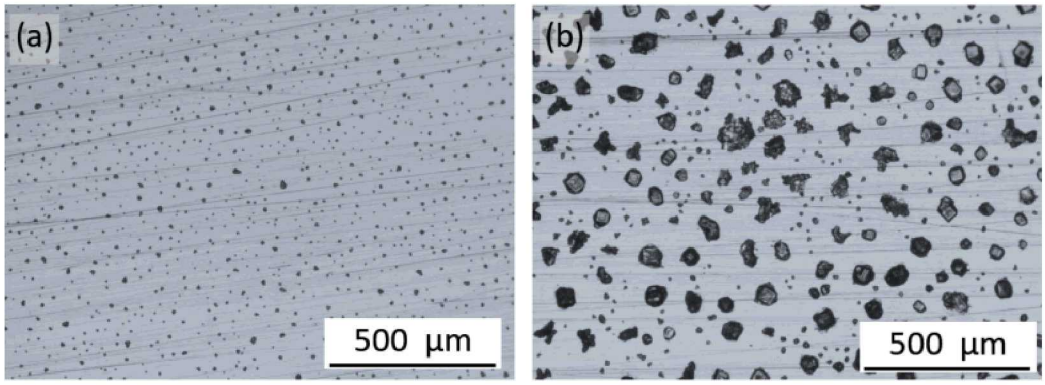

Figure 30 Sea salt particles after printing (a) 10 µg/cm^2 and (b) 300 µg/cm^2 on mirror finish 304L coupons.

The experimental matrix currently under test is given in Table 7. The values given for each time represent the number of replicate coupons for each surface finish pulled from the humidity chambers for analysis. Extra samples were included at 6 months and 18 months for leaching and chemical analysis to evaluate potential changes in the soluble salt compositions due atmospheric exchange reactions or corrosion reactions during the exposure period. The times highlighted in green are pulls that have been completed with pit morphology analysis underway. To date, samples have been pulled for up to one year of exposure.

Table 7. Experimental Matrix for Pit Characterization Experiments

Environment	Salt Load ($\mu g/cm^2$)	1 wk	2 wk	1 mo.	6 mo.	12 mo.	18 mo.	24 mo.
35°C, 75%RH	10	7	7	7	14	7	14	7
35°C, 75%RH	300	7	7	7	14	7	14	7
35°C, 40%RH	10	7	7	7	14	7	14	7
35°C, 40%RH	300	7	7	7	14	7	14	7

Figure 31 shows the typical appearance of coupons after exposure for up to 6 month with 300 $\mu g/cm^2$ at 35°C, 75%RH. Samples under these conditions exhibited the most severe corrosion. With that said, the mirror finish samples maintained their bright finish with few if any rust spots notable for up to 6 months of exposure. This contrasts with the 120 grit samples where rusting appeared within 1 week and progressively grew in coverage, following the grinding pattern, over the course of exposure. These trends are apparent for the other conditions but corrosion is much less pronounced.

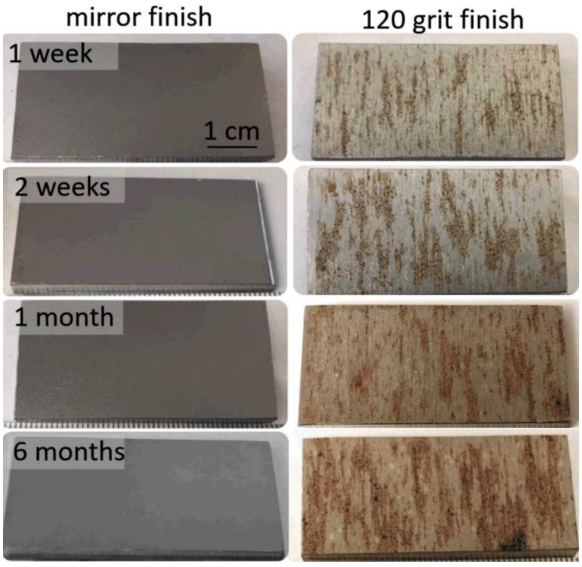

Figure 31. Appearance of 304L coupons loaded with 300 $\mu g/cm^2$ sea-salt after exposure at 35°C and 75% RH for up to 6 months.

After exposure and optical imaging, the rust is removed using a nitric acid solution and pitting damage is measured using a profilometer. To date, we have developed a semi-automated analysis process for the pit analysis. An example of the analysis procedure is given in Figure 32, whereby three 2 x 2 mm areas are measured on the coupon and pits identified. Several challenges have arisen during development of the analysis procedure. One of the major challenges is that most pits on samples exposed for up to six months have been on the size order of the surface roughness for the 120 grit samples leading to error in automated identification. Thus, each pit must be manually identified prior to automated measurement of the pit features (e.g., depth, diameter). This manual approach is prohibitively time consuming for analysis of the entire area of each sample and across the entire population. We are expecting that our automated

identification strategy may work better on samples that are exposed for longer times, given pits continue to grow. Several alternative analysis approaches are also being explored to overcome this issue.

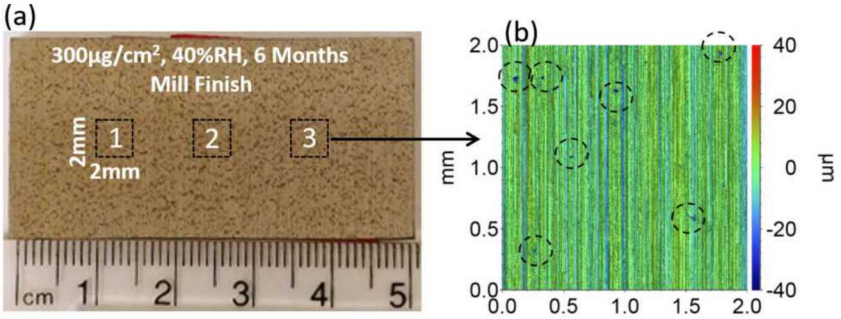

Figure 32 (a) Mill finish coupon after 6 months of exposure at 35°C, 40% RH with profilometry sample areas indicated. (b) Measured surface profile with pits identified (circles) from sample area 3. The color scale represents the surface height.

Table 8 shows pit statistics measured over time using the current analysis approach. It must be emphasized that these are initial results demonstrating proof of analysis concept and without rigorous definition of uncertainty. With that said, several trends are apparent in this data (1) the number of detectable pits on the sample are growing over time, (2) the average and maximum pit depth remained constant for up to 6 months and (3) the maximum pit diameter is increasing. Additional measurements and definition of uncertainty is necessary prior to drawing conclusions from these results. These data will be used to directly test the SNL SCC model which predicts maximum pit size over time and they will be used to develop statistical models in collaboration with CSM. Additional statistics we are collecting include pit volume and principle curvature. The latter descriptor could be utilized to determine the probability of developing a pit geometry capable creating local stress concentrations expected to initiate cracking, as will be discussed in the next section.

Table 8. Pit Statistics from 120 Grit Finish Coupons Exposed at 35°C, 40% RH and 300 µg/cm² salt load

		Pit Depth		Diameter	
Time	# of Pits	Average (µm)	Max (µm)	Average (µm)	Max (µm)
1 Week	4	15	21	24	35
2 Weeks	12	15	19	23	40
1 Month	16	15	22	29	52
6 Month	53	22	44	32	89

Efforts in FY19 will primarily focus on creation and analysis of datasets for up to 18 months exposure time. In Q1 we will expand the matrix to include a 2 year coupon exposure experiment at 40% RH, 45°C to examine the effect of temperature. In Q3 we will initiate another test under cyclic humidity conditions to capture effect of diurnal variation in ambient weather. With regard to the latter, there is no information on how cyclic conditions expected on the canisters impact pitting kinetics. The resulting datasets and analysis will be distributed to our collaborators to inform and benchmark statistical and semi-deterministic canister cracking models currently under development at SNL, CSM and OSU.

3.2 Pit-to-Crack Transition

In many susceptible alloys, corrosion pits are commonly observed as initiation sites for SCC cracks (see, for example Figure 33). Existing models for pit-to-crack transition relate pit size and shape to crack initiation through calculated stress intensity factors (Kondo, 1989; Turnbull et al., 2009; Horner et al., 2011). If the local stress intensity at the surface of a pit exceeds an empirically-determined SCC threshold stress (i.e., $K > K_{ISCC}$), a crack is assumed to initiate from that pit. The relevance of this relationship and accessible limits of these models, in general, are unknown for storage canister conditions. Furthermore, the validity of the assumption that general pit shape and size control pit-to-crack transition is not well understood. Other features, such as finer topography within pits (that could serve as stress concentrators) or microstructure could have a more commanding role in controlling pit-to-crack transition (Donahue and Burns, 2016). The aim of this work is to identify important features controlling pit-to-crack transition. Parameters of interest include pit shape, corrosion morphology (e.g. single versus satellite pits) and microstructure.

Our approach to understanding the controlling features for pit-to-crack transition and their prevalence under ISFSI-relevant conditions is to expose tensile test specimens of the same material as the coupon samples discussed in Section 3.1 to the same environmental conditions (salt load, T, and RH). During the period of exposure, the specimens will be held at a constant load with intermittent high R ripple fatigue loads applied to induce and track pit-to-crack transition. The ripple fatigue technique introduces marker bands along the crack front as it grows that can be followed, like tree rings, back to the point of crack initiation upon post-test SEM examination (Donahue and Burns, 2016). This approach will allow us to determine corrosion features that act as crack initiation sites along with the relative control of general pit shape and size. MicroCT and robotic serial sectioning are additional tools at SNL we may utilize to further characterize these specimens. These experiments will enable us to rank relative importance of pit features within the specimens. Further experiments will be carried out where controlled pits are created in tensile specimens and then tested to refine these rankings. Assuming similar behavior between the tensile specimens and the exposed coupons, we will develop statistics on prevalence of these initiation-susceptible features with respect to exposure time and environment. These statistics could be used to validate the current pit-to-crack transition models based on stress intensity factor or be used in their place as input datasets for stochastic SCC models being developed by SNL, CSM and OSU.

This task is being undertaken in collaboration with OSU. Accomplishments in FY18 include deposition of salt and exposure of tensile test specimens to the conditions given in Table 7. To date, exposures for up to six months have been completed. OSU has developed a method for periodic loading which will be demonstrated in FY19, generating data from at least one exposure condition, including identification and characterization of features controlling pit-to-crack transition.

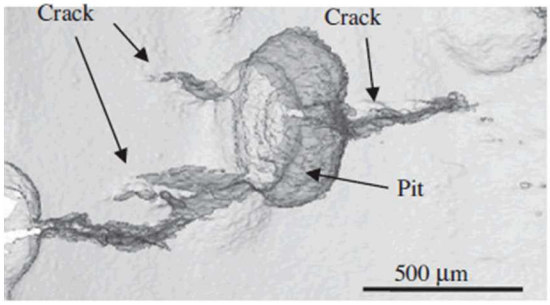

Figure 33. 3-D tomographic reconstruction of cracks emanating from a pit after exposure and mechanical loading of a 3 NiCrMoV disc. From (Horner et al., 2011).

3.3 Deterministic Linkage between Surface Environment, Damage Distributions and Rates

Confident extrapolation of stochastic canister SCC models utilizing environmental parameters as inputs and built on short term (e.g. several years) lab and field datasets to performance over decades requires mechanistic understanding of the environment-electrochemical relationship that drives pitting and SCC. Current deterministic models for atmospheric pitting and SCC provide insight into how surface environmental conditions can affect kinetics and extent of damage (Macdonald and Urquidi-Macdonald, 1991; Newman, 2002; Chen and Kelly, 2010). For example, in several SCC models, such as one proposed by Macdonald (Figure 34), the surface external to the crack acts as the cathode supplying the electrochemical driving force for crack growth. Thus, under atmospheric conditions, the surface environment (e.g., brine composition and thickness) would be expected to control damage rates. The relevance of these models as applied to SNF interim storage canisters remains largely unexplored. Furthermore, the relationship between surface state and electrochemical processes (e.g., reduction of oxygen) outside of a pit or a crack and electrochemical processes within them is not well understood. Efforts in this thrust aim to address this by quantitatively linking expected canister surface conditions to the electrochemical processes driving pitting and SCC, using existing models as initial basis for understanding.

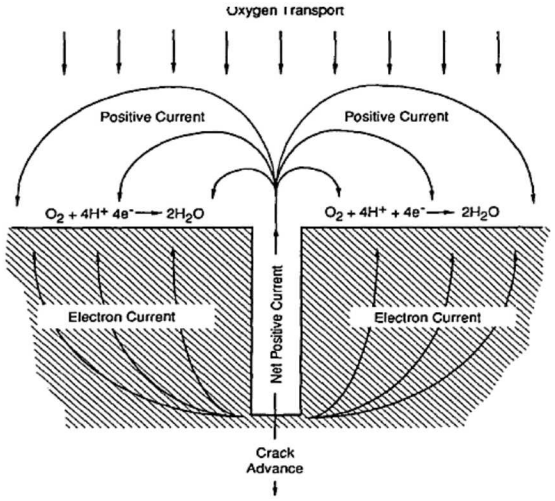

Figure 34. Conceptual schematic of electrochemical SCC model proposed by MacDonald showing coupling of oxygen reduction reaction on steel surface with internal environment. From Macdonald and Urquidi-Macdonald (1991).

Of initial interest is the impact of expected surface electrolyte physicochemical state (See Section 2) on cathodic electrochemical kinetics that drive corrosion on stainless steel surfaces. In FY18 we carried out experiments to measure the oxygen reduction reaction (ORR) kinetics on 304L and 316L in analog brines representative of chemistries and conditions expected on canisters. Oxygen reduction is the primary cathodic reaction driving corrosion processes on the canisters. To understand how electrolyte film thickness and chemistry impact the cathodic efficiency of the canister surfaces, we are measuring ORR kinetics on rotating disc stainless steel electrodes in simulated brine electrolytes. In these rotating disc experiments, the rotation speed of the electrode can be varied to control diffusion layer thickness, representative of atmospheric electrolyte layer thickness. Electrolyte chemistry and layer thickness can

be predicted from canister environmental parameters (Schindelholz et al., 2017). Datasets generated will serve as direct input for SNL's current SCC model.

Work in FY18 focused on measurements in NaCl solutions, approximating expected sea-salt brine compositions at ≥75% RH and 25 to 50°C. These conditions are at the upper bound of the predicted ISFSI relevant conditions (Table 6). The focus was not only to generate data as input for SNL's SCC model but also to develop and understanding of ORR mechanisms that enables prediction of the kinetics. The NaCl study findings are summarized in a journal paper (see Appendix A). Nonetheless, a brief summary of the type of data collected and how it is used in the SNL SCC model is provided here.

Figure 35 shows cathodic polarization curves measured on 304L at different rotation speeds (Ω) representing a range of electrolyte film thicknesses (δ). Current density proportional to the rate of oxygen reduction on the 304L electrode resultant from applying a potential across. At potentials less than the corrosion potential (where $i \rightarrow -\infty$) there is a region where log i increases linearly with decreasing potential. This is referred to as the Tafel region in which the corrosion rate is inversely proportional to the slope of the polarization curve. At even lower potentials, the current is no longer a function of potential as the reduction reaction is limited by mass transfer of oxygen to the surface. As the rotation speed is increased, the limiting current also increases. This plot demonstrates that increasing film thickness can lead to decreasing ORR rates in the oxygen diffusion limited regime.

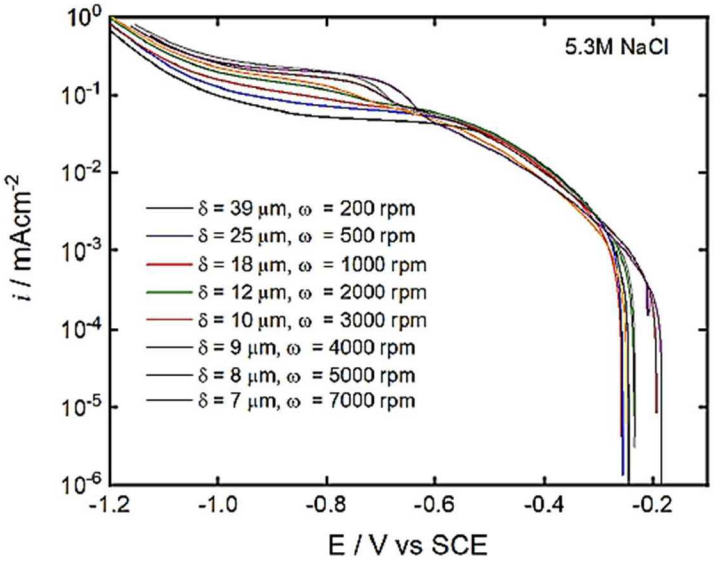

Figure 35 Cathodic polarization curves at varying electrode rotational speeds ω in saturated (5.3 M) NaCl solution at 25°C representing different brine layer thicknesses δ.

Using these data, the impact of varying surface environment on pitting damage is being explored *via* a maximum pit size model proposed by Chen and Kelly (2010). The premise of this model is that the physical and chemical properties of the brine that forms on the surface determines the maximum cathode capacity of the surface, which, in turn, can be used to determine the maximum size of a hemispherical pit that could be sustained by the cathode current.

Chen and Kelly (2010) derive the following equation for the maximum cathodic current available, $I_{c,max}$:

$$\ln I_{c,max} = \frac{4\pi k W_L \Delta E_{max}}{I_{c,max}} + ln\left[\frac{\pi e r_a^2 \int_{E_{corr}}^{E_{rp}} (I_c - I_p) dE}{\Delta E_{max}}\right] \quad \text{(Eq. 1)}$$

where
k = conductivity, Siemens/meter
W_L = brine layer thickness, meters
I_c = cathodic current density, Amps/m^2
I_p = passive current density, Amps/m^2 assumed to be 10^{-4} A/m^2 in Chen and Kelly
E_{rp} = repassivation potential = -0.4 V_{SCE} in Chen and Kelly for 304 = potential at the mouth of the pit
E_{corr} = -0.15 V_{SCE} in Chen and Kelly = E_L = potential at the cathode edge
e = Euler's number 2.71828
r_a = pit radius, meters
r_L = radius of the cathode, meters
$\Delta E_{max} = E_{corr} - E_{rp}$

Several of these parameters vary with the environmental conditions on the canister surface. These include the conductivity k, the concentration of salts in the brine m_{salt}, and the brine density ρ. These parameters vary with the RH and T at the canister surface (Schindelholz et al., 2017). The RH is equal to the activity of water in the brine, and hence, controls the concentration of salts in the brine. The temperature has a relatively minor effect on brine concentration, but has a large effect on brine density and brine conductivity. For any given environmental (T, RH) condition, the brine volume varies linearly with the salt load deposition density. The integral term on the right-hand side of the equation is determined from cathodic polarization curves, which will also potentially vary with brine layer composition and thickness. Chen and Kelly implemented a single cathodic polarization curve based on data for sea-water, measured by (Sridhar et al., 2004), and an anodic current based on the Galvele pit stability criterion. Further details and discussion of this model were reported in Bryan and Enos (2017).

Using the Chen and Kelly model, and assumptions therein, combined with cathodic kinetic data can provide predictions of the maximum hemispherical pit size possible in an NaCl rich brine, Figure 36. The data in this figure should only be taken as conceptual, given several assumptions that will be discussed below. Nevertheless, critical combinations of environmental parameters at which there is a risk of SCC can be defined through the maximum pit size model and empirical measures of electrochemical kinetics. This model is currently utilized as part of SNL's SCC modeling efforts to determine bounding pit sizes on canisters as function of environment and surface salt loading. In turn, assuming Kondo criterion, these maximum pit sizes then serve to determine conditions under which pit-to-crack transition would be most likely to occur. Similarly, conditions where cracking will not take place can also be determined. If the theoretical maximum pit size is smaller than the critical pit size required for SCC crack initiation (given the local stresses and environmental conditions that are present) then crack initiation is unlikely. Thus, if the environmental parameters and material properties for a system are known, this model can be used to map regions where there is a risk of SCC, requiring more detailed experimentation. Although of great potential utility, this model has not been benchmarked under canister-relevant conditions. It is likely that the model can only be implemented in a stochastic fashion, in which the likelihood of crack initiation increases with the predicted maximum pit size, but a minimum pit size that initiates a crack may not exist, or may be very small.

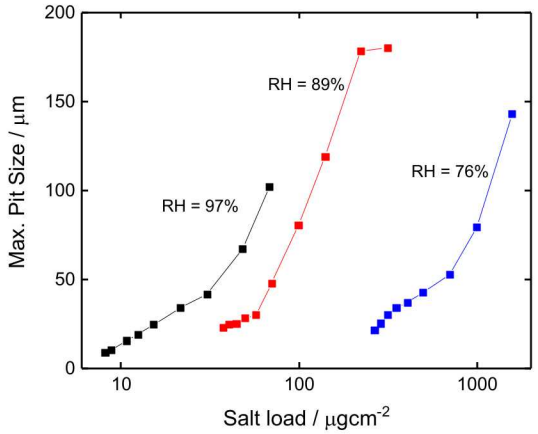

Figure 36. Conceptual calculations of maximum pit size (pit radius) based on environmentally measurable parameters.

There are several assumptions in the maximum pit size model that may result in a non-conservative conclusion and that must be addressed. These include treating the pits as hemispherical in shape, the brine layer as a uniform thin film with static properties, and assuming the material and mechanical environment (e.g., stress/strain) is homogenous. In all cases, experimental data on distribution of pit geometries at the coupon level and on the canister mock-up is critical along with understanding the effect of dynamic environment on this distribution. Regarding the latter, it is given that canister cooling, seasonal and diurnal weather cycles, continuous deposition of atmospheric particles, and reactions with atmospheric gases, result in a highly dynamic brine system (Section 2.1). Furthermore, corrosion processes can quickly (within minutes) and dramatically change the brine chemistry (Section 2.1.2). For example, we and others have demonstrated that surface chemistry at cathode sites tends towards high alkalinity due to the ORR reaction producing hydroxyl ions, and, in turn carbonates, due to reaction with atmospheric CO_2 (Schindelholz et al., 2014). Changing electrolyte properties could have considerable impact on both anodic and cathodic kinetics, and may lead to brine dry-out.

To understand the extent to which brine evolves on the surface and how, in turn, this evolution can impact cathodic corrosion kinetics, we are using surface sensitive analytical methods to map chemistry on coupons during the exposure experiments detailed in Section 3.1. Figure 37 shows the chemistry distribution on a salt-deposited coupon for up to six months exposure as measured by TOF-SIMS. In Figure 37a, the irregular Na-Cl enriched areas (red) likely represent the extent of the droplets when originally deposited onto the coupon surface. The circular Mg-Cl enriched areas (blue-green) represent the area of individual droplets when deliquesced during exposure. After one month, Figure 37b, the red and green areas become more diffuse. After six months, the area between the deliquesced droplets becomes completely covered in Na-Cl (yellow). It is clear from these results that, although discrete droplets remain over time, NaCl is diffusing across the surface likely mediated by adsorbed water layers on the steel surface. Thus, the electrolyte configuration on these coupons tends towards discrete sea-salt droplets connected by a thin film of NaCl-rich electrolyte. The thickness of this film has yet to be determined. Alkaline signatures (OH-, CO_3^{2-} and derivatives) indicative of cathodic areas were not detectable (detection limit ~ 1 ppm atoms) on these samples, nor were corrosion products visible in the analyzed areas. We hypothesize that, as corrosion develops, alkaline cathodic chemistry will become apparent and spread across the surface. The relationship between heterogeneous electrolyte distribution on a surface and corrosion damage distributions and rates is still unclear, but an important topic that will be further pursued in FY19. This will include additional measures of cathodic kinetics in expected alkaline brine chemistries. Surface chemistry characterization will continue with the coupon exposure experiments (Section3.1) in FY19.

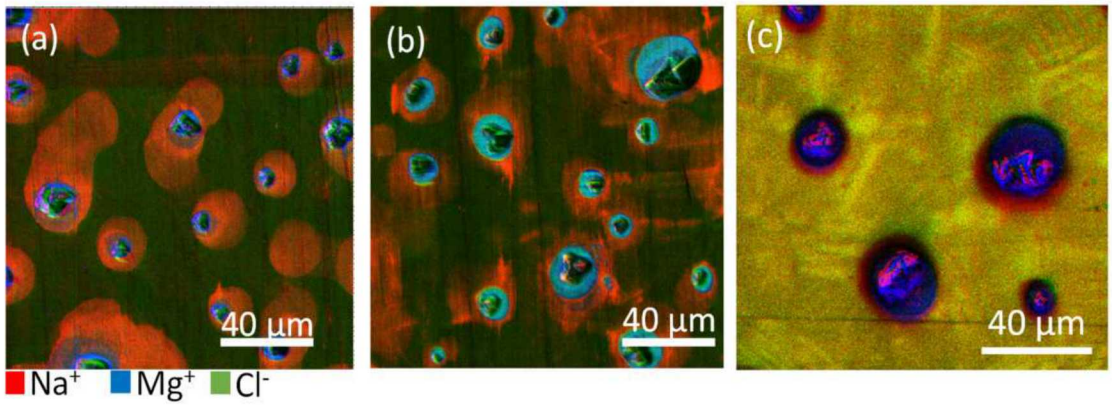

Figure 37. TOF-SIMS ion maps of sea-salt deposits on 304L stainless steel. (a) before exposure; (b) after one month; and (c) after six months exposure at 35°C, 75% RH.

4 RELATIONSHIP BETWEEN CORROSION DAMAGE, MATERIAL, AND MECHANICAL ENVIRONMENT

Quantitative information on the effect of material characteristics and mechanical environment (microstructure, composition, applied stress) on pitting damage distributions and rates, conditions of pit-to-crack transition, and crack growth are lacking under canister-relevant environments. The impact of variance of these material and mechanical environment parameters, within ranges present on the canister, on model predictions is not well understood. This thrust aims to develop a deeper understanding on how material variance impacts electrochemical corrosion processes related to SCC and resulting damage distributions and rates. Current efforts in this area are focused on two tasks: (1) determine the relative importance of canister stress levels as a parameter in pitting susceptibility; and (2), understanding crack initiation and growth behavior in relation to canister material and stress conditions using canister mock-up plate exposures. Both tasks are complimentary to CSM IRP activities.

Work in FY18 on task 1 focused on data collection and analysis of results of initial experiments to determine the relative importance of stress as a parameter in pitting susceptibility of the canisters. Stressed 304L 4-point bend specimens that were loaded with artificial sea salt and exposed for 50 days to 35%RH, 50^{o}C conditions were prepared by CSM (Figure 38a,b). Additionally, CSM provided a set of coupons of the same material (non-stressed) and exposed to the same conditions, Figure 38c. Corrosion product was cleaned from these samples and surface profilometry used to analyze corrosion pits resultant from exposure. Figure 39 shows an optical image of the cleaned areas on both a 4-point bend and a coupon that where profilometry was carried out. The frequency of pits in this area as a function of vertical location in the images (for the 4-point bend- compression to tension) are given in Figure 39. From both the histograms and optical images there are no clear trends in pit frequency as a function of stress. In other words, pit distribution was rather uniform across the stressed sample and across the unstressed coupon. Statistics on each of the pit characteristics, including pit maximum diameter, maximum depth, average depth and pit volume were measured by analyzing each pit individually. Komogorov-Smirnov (K-S) tests comparing low tension and high-tension areas on the 4-point bend sample indicate no significant difference ($\alpha = 0.01$) between the pit distributions for each of these statistics in these areas. K-S tests between the pit population on the coupon and that on the 4-point bend also show no significant difference between pit characteristics. These initial analyses suggest that stress alone did not influence pitting behavior under the conditions of the experiment, but more detailed analysis is required. Work will continue into FY19 to analyze the existing data set and additional samples. Additional experiments will be carried out across a wider parameter space (time, environmental conditions) to further characterize and understand this behavior. This will include development of electrochemical maps of regions of different stress on the 4 point bend specimen to interpret how stress impacts the electrochemical processes driving corrosion. This information and approach will serve as basis to study the pitting and SCC behavior of the more complex weld zone regions, building an electrochemical description of weld zone regions on the canister for prediction of pitting and SCC susceptible zones and informing or updating the SNL SCC model.

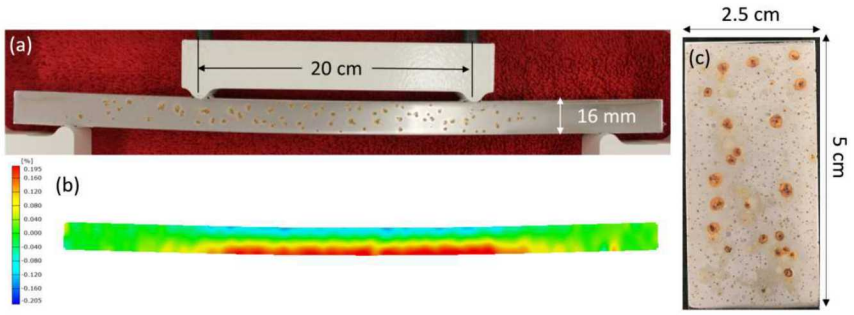

Figure 38. (a) Stressed 304L 4-point bend specimen; (b) digital image correlation stress map of the same specimen; and (c), unstressed coupon after depositing 400 µg/cm^2 sea-salt and exposing for 50 days at 50°C and 35% RH.

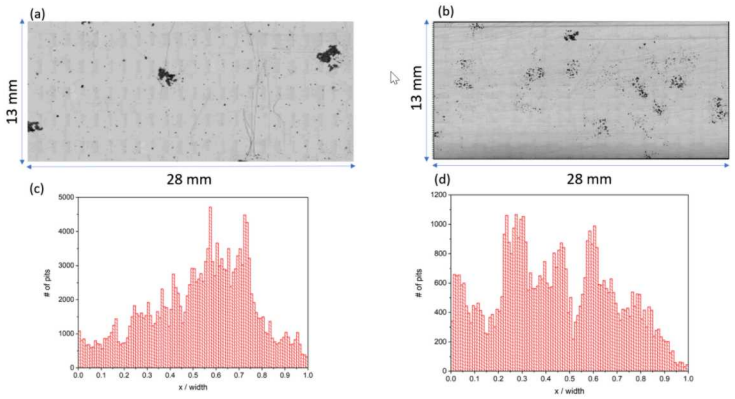

Figure 39. Images of (a) analyzed areas on a cleaned unstressed 304L coupon, and (b) a section of the stressed 4-point bend sample (b) after exposure with 400 µg/cm^2 sea salt at 50°C and 35% RH. The number of pits as a function of sample width (vertical axis in a and b) are shown in the graphs below each figure.

In FY18, we initiated exposure of a salt-loaded mockup canister plates to elevated temperature and humidity conditions to gain understanding on what portions of the canister may be most susceptible to SCC and their relationship to material condition and mechanical environment. Three large (~18" × 20") sections of the mockup canister, containing an axial weld, a circumferential weld, and a weld intersection, were loaded with ~8 g/cm^2 of $MgCl_2$ using a custom salt fog chamber. The salt-loaded plates were then placed into an environmental chamber at 80°C, 35% RH. Optical imaging and vibrothermography are being used to track the progress of cracking and corrosion at various times during exposure. Vibrothermography is an SCC detection method that is currently under development at Los Alamos National Lab (LANL) as part of the CSM-lead IRP. The principle of this technique is that high frequency vibration can cause a crack to generate heat in a material which can be picked up by thermography. The appearance of a mock-up plate before and after exposure for 5 months is shown in Figure 40. This same plate is currently at LANL for vibrothermography imaging and will be returned to the exposure conditions after imaging. Figure 41 shows the vibrothermography analysis setup and an example image of a weld zone of one of the plates prior to exposure. No cracks are apparent. Exposure of the plates will continue for up to one year or until considerable cracking becomes evident visually or through vibrothermography. After exposure (FY19Q2) more detailed analyses will be undertaken to characterize

the corrosion and SCC damage, including an attempt to identify crack initiation features. This dataset can be used to further inform and benchmark models under development and guide experimental efforts.

Figure 40. Mock-up plate section as it looked (a) before, and (b) after, $MgCl_2$ loading and exposure to 80°C, 35% RH for 2 months.

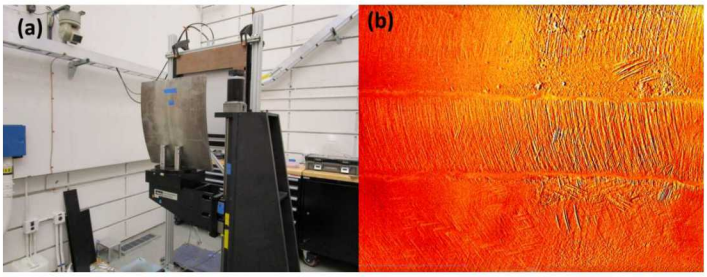

Figure 41. (a) Mock-up plate in the vibrothermography analysis fixture at Los Alamos National Lab; (b) 80khz vibrothermography image of a weld zone before exposure.

5 FY19 PLANS

Experimental efforts in FY19 will focus on continued efforts to understand the chemical environment on heated canister surfaces, and on understanding the relationship between surface environment and corrosion damage.

Research into the chemical environment will focus on the stability of sea-salt aerosols and deliquescent brines on the heated canister surface both before and after initiation of corrosion. Specific goals will be to develop an improved understanding of magnesium chloride stability and secondary phase formation in response to HCl degassing. Specifically, we will develop thermodynamic models for the magnesium chloride/magnesium hydroxychloride system and evaluate the deliquescence behavior of relevant hydroxychloride compounds. Additional work will evaluate, *via* thermodynamic modeling and experimental studies, the effects of well-known aerosol particle-gas conversion reactions on brine chemistry at elevated temperatures. These data will provide a basis for improved screening sites for SCC susceptibility.

The corrosion work will continue to focus on four thrust areas: (1) generation of temporal statistical pitting data as function of environment; (2) hierarchal identification of features controlling pit-to-crack transitions; (3) definition of the surface environment-electrochemical relationship driving pitting and SCC; (4) definition of relative governance on material condition and stress relative to surface environmental conditions on electrochemical kinetics and SCC susceptibility.

Regarding (1), pit datasets will be generated from measurements on 304L coupons exposed to ISFSI-relevant isohumidity conditions for up to 18 months (continuing from FY17 experiments). An elevated temperature exposure will be initiated to capture the upper temperature bound of expected ISFSI corrosive conditions. A cyclic humidity exposure representative of diurnal weather patterns will also be initiated to understand the effect of dynamic RH on pit initiation and growth. Furthermore, the relationship between heterogeneous electrolyte distribution on a surface and corrosion damage distributions and rates t will be pursued in FY19. Continued collaboration with OSU and CSM is planned.

Data for (2) will be generated for at least one exposure condition from tensile specimens prepared in FY18, including identification of characteristic features controlling pit-to-crack transition. Hydraulic load frames purchased in FY 18 will be installed at SNL and utilized for these FY19 efforts. Furthermore, provided stable cracks can by successfully initiated, we will attempt to measure crack growth rates on these specimens. Continued collaboration with OSU is planned.

Measurements of oxygen reduction reaction (ORR) cathodic kinetics on 304L and 316L in analog brines representative of chemistries and conditions expected on canisters will continue in FY19 under thrust (3). Specifically, measurements will be made in $MgCl_2$ brines analogous to low RH sea salt brines and also artificial sea salt brines at range of temperature and RH capturing ISFSI environmental space. Furthermore, the effect of ORR processes and atmospheric interaction on cathodic, and in turn, corrosion kinetics will be initially explored using the rotating disc electrode approach. Datasets generated will be input into SNL's SCC model.

Work in thrust (4) will include analysis of additional 4-point bend specimens provided by CSM to understand how stress impact pitting behavior. This will include development of electrochemical maps of regions of different stress on the 4-point bend specimen to elucidate its effect on electrochemical processes driving corrosion. This information and approach will serve as basis to study the pitting and SCC behavior of the more complex weld zone regions, building an electrochemical description of weld zone regions on the canister for prediction of pitting and SCC susceptible zones and informing or updating the SNL SCC model. Finally, will continue to characterize salt-loaded mock-up plates over the course of long-term exposure to characterize localized corrosion and SCC behavior.

Finally, in FY19, SNL will begin to evaluate the environmental dependencies of SCC crack initiation and growth rates using SCC tensile specimens and load frames with environmental chambers enclosing the samples. The load frames were purchased in FY18, and are in the process of being installed at SNL.

6 CONCLUSIONS

This progress report describes work done in FY18 at Sandia National Laboratories (SNL) to assess the localized corrosion performance of container/cask materials used in the interim storage of spent nuclear fuel (SNF). Of particular concern is stress corrosion cracking (SCC), by which a through-wall crack could potentially form in a canister outer wall over time intervals that are shorter than possible dry storage times. Work in FY18 refined our understanding of the chemical and physical environment on canister surfaces, and evaluated the relationship between chemical and physical environment and the form and extent of corrosion that occurs.

Work to define the chemical and physical environment that could develop on storage canister surfaces in near-marine environments included experiments to evaluate the thermal stability of magnesium chloride brines, representative of the first brines to form when sea-salts deliquesce, with the specific goal of understanding and interpreting results of sea-salt and magnesium chloride corrosion experiments carried out under accelerated conditions. The experiments showed that magnesium chloride brines, and by extension, low RH sea-salt deliquescent brines, are not stable at elevated temperatures, losing chloride via degassing of HCl and conversion to Mg-hydroxychlorides and carbonates. The experiments were carried out on an inert substrate to eliminate the effects of corrosion reactions, simulating brine stabilities in the absence of, or prior to, corrosion. Moreover, analysis of salts recovered from actively corroding metal samples shows that shows that corrosion also supports or drives conversion of magnesium chloride or sea-salt brines to less deliquescent salts. This process has significant implications on corrosion, as the secondary phases are less deliquescent than magnesium chloride; the conversion reaction results in decreases in brine volume, and potentially ultimately results in brine dry-out. The deliquescence properties of these reaction products will be a topic of active research in FY19.

In FY18, Sandia also continued its multi-year study of salts deposited on the surface of in-service SNF interim storage canisters, obtaining and analyzing dust samples from the Maine Yankee site. Soluble salts were present in significant amounts in the dust, and were dominated by sulfates and nitrates. However, chloride was present in significant amounts, occurring as sodium chloride and commonly associated with coarse plant fibers and pollen in the dust, and with fine aggregates of silicate minerals, likely clays. Sea-salt aerosols were not observed. The association of chloride salts with other particulates must be considered when evaluating salt transport and deposition phenomena both externally and within the overpack, as the aerodynamic properties of the materials will vary from those of standard sea-salt aerosols or deliquesced droplets. The composition of the soluble component was relatively consistent in the six samples collected, although the amount present varied. The composition and relative species concentrations (ion ratios) indicate that sea-salts alone cannot account for the observed salts, and that a large component of continental-salt aerosols is present. Measured chloride surface loads are low, with the highest values being less than 0.1 g/m^2. Salt load is an important risk factor for SCC, and while values this low have been known to cause SCC, these low salt loads are a positive factor. The potential role of the other soluble components in mitigating or increasing SCC risk is not known.

Experimental efforts in FY18 to understand the relationship between surface environment and corrosion damage focused on four thrust areas: (1) generation of temporal statistical pitting data as function of environment; (2) hierarchal identification of features controlling pit-to-crack transitions; (3) definition of the surface environment-electrochemical relationship driving pitting and SCC; (4) definition of relative governance on material condition and stress relative to surface environmental conditions on electrochemical kinetics and SCC susceptibility. FY18 work in area (1) continued with characterization of pitting damage and surface chemistry on 304L coupons loaded with sea-salt and exposed to ISFSI-relevant fixed RH,T conditions. To date, samples exposed for up to 1 year have been generated. In collaboration with Ohio State University (OSU), we have demonstrated a semi-automated pit measurement approach based on optical profilometry and generated initial pit datasets for coupon exposure times up to 6 months. These data will be used to directly test the SNL SCC model and develop

statistical models in collaboration with Colorado School of Mines (CSM). Regarding (2), and in collaboration with OSU, experiments have been initiated to identify pit-to-crack transition features. Accomplishments include deposition of salt and exposure of tensile test specimens to the environmental conditions used in thrust (1) for up to six months. Additionally, we have developed and tested a method for periodic loading of the specimens while under said environments. Regarding (3), the cathodic electrochemical kinetics that drive corrosion on stainless steel were measured for NaCl brines as analogs to expected brines compositions on the canisters at the upper end of expected ISFSI surface humidity range. These data were incorporated into SNL's SCC model and findings communicated in a peer-reviewed journal publication. Work in area (4) included completion of 4-point bend experiments using stressed 304L bars loaded with sea salt and exposed to 35%RH, 50^{o}C conditions in collaboration with CSM. The pit distribution on one of these bars was analyzed via optical profilometry with initial results suggesting pit frequency, depth and diameter was independent on material stress state within expected canister conditions. Finally, we initiated exposure of a salt-loaded mockup canister plates to elevated RH, T conditions to gain understanding on what portions of the canister may be most susceptible to SCC and their relationship to material condition and mechanical environment.

7 REFERENCES

ASTM International. (2008). *D1141-98: Standard Practice for the Preparation of Substitute Ocean Water.* American Society for Testing and Materials, p.

Bryan, C. and Enos, D. (2014). *Analysis of Dust Samples Collected from Spent Nuclear Fuel Interim Storage Containers at Hope Creek, Delaware, and Diablo Canyon, California.* SAND2014-16383. Sandia National Laboratories, 281 p.

Bryan, C. and Enos, D. (2015a). *Analysis of Dust Samples Collected from an Unused Spent Nuclear Fuel Interim Storage Container at Hope Creek, Delaware.* SAND2015-1746. Sandia National Laboratories, 131 p.

Bryan, C. and Enos, D. (2015b). *SNF Interim Storage Canister Corrosion and Surface Environment Investigations.* FCRD-UFD-2015-00511. U.S. Department of Energy, 79 p.

Bryan, C. and Enos, D. (2016). *Analysis of Dust Samples Collected from an In-Service Interim Storage System at the Maine Yankee Nuclear Site.* SAND2016-10266. Sandia National Laboratories, 51 p.

Bryan, C. and Enos, D. (2017). *FY16 Status Report: SNF Interim Storage Canister Corrosion and Surface Environment Investigations.* FCRD-UFD-2016-00429. U.S. Department of Energy, 86 p.

Burstein, G. and Pistorius, P. (1995). Surface roughness and the metastable pitting of stainless steel in chloride solutions. *Corrosion* **51**, 380-385.

Chen, Z. and Kelly, R. (2010). Computational modeling of bounding conditions for pit size on stainless steel in atmospheric environments. *Journal of the Electrochemical Society* **157**, C69-C78.

Crisp, T. A., Lerner, B. M., Williams, E. J., Quinn, P. K., Bates, T. S. and Bertram, T. H. (2014). Observations of gas phase hydrochloric acid in the polluted marine boundary layer. *Journal of Geophysical Research: Atmospheres* **119**, 6897-6915.

de Bakker, J., LaMarre, J., Peacey, J. and Davis, B. (2012). The phase stabilities of magnesium hydroxychlorides. *Metallurgical and Materials Transactions B* **43**, 758-763.

Donahue, J. R. and Burns, J. T. (2016). Effect of chloride concentration on the corrosion–fatigue crack behavior of an age-hardenable martensitic stainless steel. *International Journal of Fatigue* **91**, 79-99.

dos Anjos, A. P. A., Sifeddine, A., Sanders, C. J. and Patchineelam, S. R. (2011). Synthesis of magnesite at low temperature. *Carbonates and Evaporites* **26**, 213-215.

Enos, D. and Bryan, C. (2016a). *Final Report: Characterization of Canister Mockup Weld Residual Stresses.* FCRD-UFD-2016-000064. U.S. DOE, 62 p.

Enos, D. and Bryan, C. (2016b). Understanding the Risk of Chloride Induced Stress Corrosion Cracking of Interim Storage Containers for the Dry Storage of Spent Nuclear Fuel: Evolution of Brine Chemistry on the Container Surface. *CORROSION 2016.* Vancouver, B.C.: NACE International.

Enos, D. G., Bryan, C. R. and Norman, K. M. (2013). *Data Report on Corrosion Testing of Stainless Steel SNF Storage Canisters.* FCRD-UFD-2013-000324. U.S. Department of Energy, Office of Used Nuclear Fuel Disposition, 103 p.

EPRI. (2011). *Extended Storage Collaboration Program (ESCP) Progress Report and Review of Gap Analyses.* 234 p.

EPRI. (2014). *Calvert Cliffs Stainless Steel Dry Storage Canister Inspection.* 460 p.

EPRI. (2015). *Susceptibility Assessment Criteria for Chloride-Induced Stress Corrosion Cracking (CISCC) of Welded Stainless Steel Canisters for Dry Cask Storage Systems.* Electric Power Research Institute, 206 p.

Hanson, B., Alsaed, H., Stockman, C., Enos, D., Meyer, R. and Sorenson, K. (2012). *Gap analysis to support extended storage of used nuclear fuel.* FCRD-USED-2011-000136. U.S. Department of Energy, 218 p.

Harris, G., Klemp, D. and Zenker, T. (1992). An upper limit on the HCl near-surface mixing ratio over the Atlantic measured using TDLAS. *Journal of atmospheric chemistry* **15**, 327-332.

Horner, D., Connolly, B., Zhou, S., Crocker, L. and Turnbull, A. (2011). Novel images of the evolution of stress corrosion cracks from corrosion pits. *Corrosion Science* **53**, 3466-3485.

Kondo, Y. (1989). Prediction of fatigue crack initiation life based on pit growth. *Corrosion* **45**, 7-11.

Kulmala, M., Toivonen, A., Mattila, T. and Korhonen, P. (1998). Variations of cloud droplet concentrations and the optical properties of clouds due to changing hygroscopicity: A model study. *Journal of Geophysical Research: Atmospheres* **103**, 16183-16195.

Macdonald, D. D. and Urquidi-Macdonald, M. (1991). A coupled environment model for stress-corrosion cracking in sensitized Type-304 stainless-steel in LWR environments. *Corrosion Science* **32**, 51-81.

Moayed, M. H., Laycock, N. and Newman, R. (2003). Dependence of the critical pitting temperature on surface roughness. *Corrosion Science* **45**, 1203-1216.

Möller, D. (1990). The Na/Cl ratio in rainwater and the seasalt chloride cycle. *Tellus B* **42**, 254-262.

Montes-Hernandez, G., Renard, F., Chiriac, R., Findling, N. and Toche, F. (2012). Rapid precipitation of magnesite microcrystals from Mg (OH) 2-H2O-CO2 slurry enhanced by NaOH and a heat-aging step (from~ 20 to 90 C). *Crystal Growth & Design* **12**, 5233-5240.

Newman, J. and Raju, I. (1981). An empirical stress-intensity factor equation for the surface crack. *Engineering Fracture Mechanics* **15**, 185-192.

Newman, J. C. and Raju, I. S. (1979). *Analysis of Surface Cracks in Finite Plates Under Tension or Bending Loads.* Technical Paper 1578 NASA, p.

Newman, R. C. (2002). Stress-corrosion cracking mechanisms. *CORROSION TECHNOLOGY-NEW YORK AND BASEL-* **17**, 399-450.

NRC. (2012). *Potential Chloride Induced Stress Corrosion Cracking of Austenitic Stainless Steel and Maintenance of Dry Cask Storage System Canisters.* NRC Information Notice 2012-20, November 14, 2012. U.S. NRC, p.

NRC. (2014). *Identification and Prioritization of the Technical Information Needs Affecting Potential Regulation of Extended Storage and Transportation of Spent Nuclear Fuel.* U.S. Nuclear Regulatory Commission, 138 p.

NWTRB. (2010). *Evaluation of the Technical Basis for Extended Dry Storage and Transportation of Used Nuclear Fuel.* NWTRB, 145 p.

Sayles, F. and Fyfe, W. (1973). The crystallization of magnesite from aqueous solution. *Geochimica et Cosmochimica Acta* **37**, 87IN197-196IN299.

Schaller, R. F., Jove-Colon, C. F., Taylor, J. M. and Schindelholz, E. J. (2017). The controlling role of sodium and carbonate on the atmospheric corrosion rate of aluminum. *npj Materials Degradation* **1**, 20.

Schindelholz, E., Bryan, C. and Alexander, C. (2017). *FY17 Status Report: Research on Stress Corrosion Cracking of SNF Interim Storage Canisters.* SFWD-SFWST-2017-000003. U.S. Department of Energy, 59 p.

Schindelholz, E. and Kelly, R. (2010a). Application of inkjet printing for depositing salt prior to atmospheric corrosion testing. *Electrochemical and Solid-State Letters* **13**, C29-C31.

Schindelholz, E. and Kelly, R. G. (2010b). Application of Inkjet Printing for Depositing Salt Prior to Atmospheric Corrosion Testing. *Electrochemical and Solid State Letters* **13**, C29-C31.

Schindelholz, E., Risteen, B. and Kelly, R. (2014). Effect of Relative Humidity on Corrosion of Steel under Sea Salt Aerosol Proxies I. NaCl. *Journal of the Electrochemical Society* **161**, C450-C459.

SNL. (2007). *In-drift precipitates/salts model.* ANL-EBS-MD-000045 REV 03. Sandia National Laboratories, 358 p.

Sridhar, N., Brossia, C., Dunn, D. and Anderko, A. (2004). Predicting localized corrosion in seawater. *Corrosion* **60**, 915-936.

Suffield, S., Fort, J. A., Cuta, J. M. and Adkins, H. E. (2012). *Thermal Modeling of NUHOMS HSM15 Storage Module at Calvert Cliffs Nuclear Power Station ISFSI.* FCRD-UFD-2012-000114. U.S. Department of Energy, p.

Turnbull, A., Horner, D. and Connolly, B. (2009). Challenges in modelling the evolution of stress corrosion cracks from pits. *Engineering Fracture Mechanics* **76**, 633-640.

Turnbull, A., McCartney, L. and Zhou, S. (2006). Modelling of the evolution of stress corrosion cracks from corrosion pits. *Scripta materialia* **54**, 575-578.

Vierkorn-Rudolph, B., Bächmann, K., Schwarz, B. and Meixner, F. (1984). Vertical profiles of hydrogen chloride in the troposphere. *Journal of atmospheric chemistry* **2**, 47-63.

Wolery, T. W. and Jarek, R. L. (2003). *Software User's Manual, EQ3/6 Version 8.0.* Sandia National Laboratories, p.

This page is intentionally left blank.

APPENDIX A

Journal Article: Oxygen Reduction on Stainless Steel in Concentrated Chloride Media

This page is intentionally left blank.

Journal of The Electrochemical Society, **165** (13) C869-C877 (2018) C869

Oxygen Reduction on Stainless Steel in Concentrated Chloride Media

Christopher L. Alexander,[1,*] Chao Liu,[2,] Ali Alshanoon,[2,**] Ryan M. Katona,[2,**] Robert G. Kelly,[2,***] Jacob Carpenter,[1] Charles Bryan,[1] and Eric Schindelholz[1,*,z]**

[1]*Materials Science and Engineering, Sandia National Laboratories, Albuquerque, New Mexico, USA*
[2]*Materials Science and Engineering, University of Virginia, Charlottesville, Virginia, USA*

In this work, a rotating disk electrode was used to measure the cathodic kinetics on stainless steel as a function of diffusion layer thickness (6 to 60 μm) and chloride concentration (0.6 to 5.3 M NaCl). It was found that, while the cathodic kinetics followed the Levich equation for large diffusion layer thicknesses, the Levich equation overpredicts the mass-transfer limited current density for diffusion layer thicknesses less than 20 μm. Also, an unusual transitory response between the activation and mass-transfer controlled regions was observed for small diffusion layer thicknesses that was more apparent in lower concentration solutions. The presence and reduction of an oxide film and a transition in the oxygen reduction mechanism were identified as possible reasons for this response. The implications of these results on atmospheric corrosion kinetics under thin electrolyte layers is discussed.
 [DOI: 10.1149/2.0181813jes]

Manuscript submitted July 16, 2018; revised manuscript received September 4, 2018. Published September 13, 2018.

Oxygen reduction reaction (ORR) processes on stainless steel (SS) are fundamentally important across a broad range of science and technology areas, including fuel cells, chlor-alkali processing, and corrosion. For the latter case, ORR is typically the primary cathodic reaction on SS under freely corroding conditions in neutral aerated chloride media.[1] ORR cathodic kinetics can control both the rate and extent of localized corrosion under these conditions.[2] For example, in saline atmospheric environments, such as marine locations, corrosion occurs under thin (typically <500 μm) highly concentrated electrolyte films.[3] When the film thickness is less than the natural convection boundary layer thickness, ORR kinetics, and in turn corrosion kinetics, can be dependent on film thickness (O_2 diffusion path length to the surface) and salt concentration in the film (O_2 solubility) amongst other factors.[4–7] Motivated by this relationship and to extend current knowledge of ORR kinetics to more extreme chloride media conditions, this study examines ORR kinetics on austenitic stainless steel and platinum electrodes under varying diffusion boundary layer thicknesses in highly concentrated sodium chloride solutions.

Numerous studies of ORR on stainless steel alloys in aerated chloride media provide a general picture of kinetic characteristics and the strong influence on the state of the native oxide film. Rotating disk electrode (RDE) studies have demonstrated ORR on 304L and 316L stainless steels to obey Levich behavior with first order reaction kinetics for diffusion boundary layer thicknesses down to approximately 15 μm for chloride concentrations of 0.5 M and Tafel slopes ranging from −115 to −180 mV/dec.[8] Gojkovic et al.[9] studied ORR on a duplex stainless steel in 0.5 M NaCl at neutral and alkaline pH and also observed Levich behavior down to approximately 15 μm and Tafel slopes of approximately −150 mV/dec. Le Bozec et al.[10] studied oxygen reduction on 316L and 904L in seawater and showed that the reaction mechanism includes partial reduction to hydrogen peroxide because the number of electrons transferred was between 2 and 4.

In terms of the effect of oxide properties or surface state, Le Bozec et al.[10] showed that ORR is strongly dependent on the pretreatment method of the surface. For prereduced surfaces, ORR follows the 4–electron pathway and is mass-transfer limited. For polished surfaces, ORR follows both the 2– and 4–electron pathways and is also mass-transfer limited. On passive surfaces, ORR occurs simultaneously with oxide reduction and ORR is not mass-transfer limited. Babic et al.[8] studied oxygen reduction on 304L in de-aerated electrolytes and observed that the oxide film reduction occurs in the same potential range as oxygen reduction.

Information to date, however, is lacking regarding ORR behavior on SS in highly concentrated brines (>1 M to saturation) and thinner boundary layers (<15 μm) representative of conditions typical for saline electrolyte brines on atmospherically exposed surfaces or, possibly, flowing systems. The objective of this work was to extend the current understanding of ORR kinetics on stainless steel to concentrated saline electrolytes and across a range of diffusion boundary layer thicknesses. Specifically, we are interested in how highly concentrated chloride media may affect the ORR pathway given the known strong interaction of chloride with the native oxide under these conditions.

This work presents oxygen reduction kinetics on 304L, 316L, and platinum in 0.6 to 5.3 M (saturated) NaCl solutions across a range of boundary layer thickness achievable via a rotating disk electrode. The strong effect of the state of the oxide film and also diffusion layer thickness on oxygen reduction kinetics will be demonstrated and discussed.

Experimental

Rotating disk electrodes of diameter 5 mm and comprised of 304L (UNS# S30403), 316L (UNS# S31603), and 99.99% platinum were acquired from Pine Research Instrumentation, Inc. (USA). Prior to each use, the electrodes were polished using 1 μm diamond paste, then rinsed with ultrapure (18.2 MΩ-cm) water, then with isopropyl alcohol, and then again with ultrapure water. The electrodes were immediately used following the polishing procedure. Sodium chloride solutions were prepared using ultrapure water and sodium chloride (ACS reagent ≥ 99.0%).

In all measurements, the rotating disk electrode (RDE) was placed in the NaCl solution at the specified rotation speed for 1 hour at open circuit potential (OCP) prior to each measurement. Cathodic polarization curves were obtained by sweeping potential from the OCP to −1.2 V_{SCE} at a scan rate of 0.167 mV/s unless stated otherwise. Temperature was controlled to 25 ±1°C using jacketed cells with a heated water circulator. A glass frit was used to bubble in lab air to maintain saturated oxygen concentration measured using a Thermo Scientific (USA) Orion RDO dissolved oxygen probe before and after the experiment. Replicate measurements were made for 1 M NaCl solutions and select diffusion layer thicknesses for higher concentration solutions to ensure the observed trends were consistent. Where applicable, replicate measurements are presented in the figures.

Results and Analysis

The influence of chloride concentration and diffusion layer thickness on oxygen reduction kinetics was studied by comparing cathodic

[*]Electrochemical Society Member.
[**]Electrochemical Society Student Member.
[***]Electrochemical Society Fellow.
[z]E-mail: ejschi@sandia.gov